OPTIMIZATION OF POLARIZATION AND INCIDENCE ANGLES CONFIGURATION FOR ESTIMATION OF SURFACE ROUGHNESS IN SLOPING AREAS USING ENVISAT-1 ASAR DATA

Rajiv R. K. Nair
January, 2007

OPTIMIZATION OF POLARIZATION AND INCIDENCE ANGLES CONFIGURATION FOR ESTIMATION OF SURFACE ROUGHNESS IN SLOPING AREAS USING ENVISAT-1 ASAR DATA

by

Rajiv R. K. Nair

Thesis submitted to the International Institute for Geo-information Science and Earth Observation in partial fulfilment of the requirements for the degree of Master of Science in Geo-information Science and Earth Observation, with specialisation in Geoinformatics

Thesis Assessment Board
Prof. Dr. Alfred Stien (ITC, The Netherlands)
Prof. Dr. S.K. Bartaria (WIHG, Dehradun)
Mr. P.L.N. Raju (IIRS, Dehradun)
Mr. C. Jeganathan (IIRS, Dehradun)

Thesis Supervisors
IIRS   : Dr. Sameer Saran
ITC   : Dr. Valentyn Tolpekin

iirs

**INTERNATIONAL INSTITUTE FOR GEO-INFORMATION SCIENCE AND EARTH OBSERVATION
ENSCHEDE, THE NETHERLANDS
&
INDIAN INSTITUTE OF REMOTE SENSING, NATIONAL REMOTE SENSING AGENCY (NRSA),
DEPARTMENT OF SPACE, GOVT. OF INDIA, DEHRADUN, INDIA**

Disclaimer

Abstract

Natural processes such as the production of soil occur at an alarmingly slower rate than soil can be lost. Erosion from productive croplands decreases soil quality and crop production, diminishes on-site land value, and causes off-site environmental damage. To protect the land from further degradation and make the mitigation measures effective, it is essential to know the spatial distribution of the areas susceptible to degradation and to assess erosions hazard severity. There are many models that are used for the prediction of soil erosion, for those who plan soil conservation systems, conduct environmental planning, or assess offsite impacts caused by wind or water erosion. Most of these models have surface roughness indices as input parameters, which require strenuous field observations. This restricts the applications of such models to small catchments. In this regard satellite data, especially ASAR data covering large areas can be considered as an alternative source for deriving these indices.

With the aim at developing a basis for a better estimation of roughness parameters in slopping terrain, using either theoretical or physical based inversion models of estimation, the present study attempts at deriving an optimal configuration of incidence angle and polarization for estimation of roughness indices in slopping areas using ENVISAT ASAR datasets. ENVISAT ASAR operating with 5.33 GHz bandwidth offers repeat measurements with a minimum duration of 5 days between two successive images at different incidence angles ranging from 15° to 45.2^o, as compared to 35 days for ERS and SAR. It also facilitates the acquisition of images with the option of selection of two simultaneous polarizations from the four polarizations HH, HV, VH, and VV.

For the study three incidence angle ranges of IS-2($19.2 - 26.7^0$), IS-4($31.0 - 36.3^0$) and IS-6($39.1 - 42.8^0$) at four polarization configurations of HH, HV, VH and VV were taken into consideration. The backscattering coefficients for the datasets were estimated taking into consideration the local incidence angles that were derived from a level-5 aster DEM. The generated Level-5 aster DEM exhibited an RMSE height error of 8.45 meters on validation with GCPs. The derived Backscattering coefficients were then analysed with field measured surface roughness measures (RMS surface height variations and the RMS crop height variations) and volumetric soil moisture contents using correlation and regression techniques. For the post-monsoon datasets, the results of the study indicate that for the cross polarization VH there exists a positive correlation (R= 0.7) between the measured surface variations and estimated dB values at swath range IS-2 ($19.2 - 26.7^0$). A linear increase in the dB values with increase in the surface roughness was observed for slopping areas.

For the measured crop height observations as an indicator for surface roughness, correlation between the RMS crop heights and derived dB values were found in like polarization VV (R= 0.7) for swath IS-2 ($19.2 - 26.7^0$) and HH (R= 0.8) for swath IS-4 ($31.0 - 36.3^0$). A linear increase in backscattering coefficients with increasing crop height was observed. Correspondingly a similar correlation was also observed between HH (R= 0.8) for swath IS-4 ($31.0 - 36.3^0$) and measured volumetric moisture contents. A ratio of backscattering coefficients at HH polarization for swath IS-4 to the backscattering coefficients at VV polarization for swath IS-2 is expected to give a better discrimination for estimations of soil moisture contents in slopping areas.

Key words: Surface Roughness, ENVISAT ASAR, Polarization, Local Incidence angle, Optimization, Hilly terrain.

Acknowledgements

Table of contents

List of figures

List of tables

1. Introduction

1.1. Background on soil erosion

Today's society often times focuses on sensational news and short-term crises, which surround us. By constantly dwelling in the present, many people ignore the long-term problems that compound slowly until they reach a crisis level, and may then be very difficult or impossible to correct. One such continuing long-term problem is soil erosion. Natural processes such as the production of soil occur at an alarmingly slower rate than soil can be lost. The agents of soil erosion are water and wind, each contributing to a significant amount of soil loss each year. The main variables affecting soil erosion due to water are precipitation and surface runoff. Raindrops, the most common form of precipitation, can be very destructive when they strike bare soil. When raindrops impact with soil they splash grains of soil into the air and wash out seeds. Overland flow, or surface runoff, then carries away the detached soil, and may detach additional soils and then sediment which can be deposited elsewhere. Soil erosion may be a slow process that continues relatively unnoticed, or it may occur at an alarming rate causing serious loss of topsoil. The loss of soil from farmland may be reflected in reduced crop production potential, lower surface water quality and damaged drainage networks.

1.1.1. Factors governing soil erosion due to water

The rate and magnitude of soil erosion by water is governed by the following factors, rainfall Intensity and runoff. Both rainfall and runoff factors must be considered in assessing a water erosion problem. Runoff can occur whenever there is excess water on a slope that cannot be absorbed into the soil or trapped on the surface. The amount of runoff can be increased if infiltration is reduced due to soil compaction, crusting or freezing. Runoff from the agricultural land may be greatest when the soils are usually saturated and vegetative cover is minimal.

In many parts of the world excess runoff and soil erosion are the major sources of damage in agricultural areas. Surface runoff occurs when rainfall intensity exceeds the soil infiltration capacity (Zobeck and Onstad, 1987). Soil scientists believe soil surface roughness plays an important role in trapping water and promoting infiltration rates as well as reducing the down stream surface runoff. Soil surface roughness has been seen to significantly impact runoff and erosion under rainfall. A common perception is that runoff and erosion decreases as a function of roughness because of surface ponding and increased hydraulic roughness that reduces effective flow shear stress. Studies conducted by (Gómeza and Nearingb, 2005) show that the surface roughness had a significant influence in delaying the runoff in the initial stages. Also erosion was greater on the rougher slope at 5% steepness, probably due to concentration of flow as it moved around the roughness elements on the rougher slope. Therefore the mapping of soil roughness states could offer a reliable key for assessing which surfaces could potentially contribute to significant runoff.

1.1.2. Need for Erosion Prediction

Erosion from productive croplands decreases soil quality and crop production, diminishes on-site land value, and causes off-site environmental damage. To protect the land from further degradation and make the mitigation measures effective, it is essential to know the spatial distribution of the areas

susceptible to degradation and to assess erosions hazard severity. There are many models that are used for the prediction of soil erosion, for those who plan soil conservation systems, conduct environmental planning, or assess offsite impacts caused by wind or water erosion. Surface properties, such as random and oriented roughness are accounted for in the Wind Erosion Prediction System (WEPS) SOIL submodel. The Water Erosion Prediction Project (WEPP) model also accommodates the spatial and temporal variability in surface roughness. For most of these models the input of surface roughness indices requires field observations, which restrict the applications of such models to small catchments. In this regard satellite data covering large areas can be considered as an alternative input for such models.

1.1.3.   Scope of Remote sensing and GIS in Erosion Prediction

Estimation of land surface parameters from imaging radar had been of interest in recent past. Estimation of soil moisture, surface roughness and vegetation parameters from satellite measurements is of primary importance for agricultural, hydrology and meteorological applications. In order to retrieve this information, there is a need to examine the influence of various surface properties on microwave response . Active microwave remote sensing offers an opportunity for retrieval of soil moisture as well as surface roughness information through spaceborne imaging radar satellites. The information obtained can be used for diverse applications such as soil erosion studies and many more. However, the contribution of surface roughness on the radar backscattered signal needs to be estimated accurately, since both soil moisture and soil roughness influence radar backscatter from soil surfaces.

1.2.   Radar fundamentals

RADAR, is an acronym for "Radio Detection And Ranging". It is an active sensor that transmits and receives electromagnetic energy in the microwave range . The majority of current operational imaging radars use wavelengths between 1 mm to 1 m. Two distinctive features characterize microwave wavelengths from a remote sensing point of view: (i) microwaves are capable of penetrating the atmosphere under virtually all conditions, and (ii) microwave reflections or emissions from surface materials bear no direct relationship to reflectance in the visible or thermal portions of the spectrum (Lillesand and Kiefer, 2000). Some of the concepts of imaging radar remote sensing considered important for understanding their applications to the study of surface roughness are mentioned in the sections to follow.

1.2.1.   Radar operation

Radar remote sensing of the land is made possible by the high atmospheric transmission in the microwave range of the electromagnetic spectrum (figure 1.1). Being an active sensor, a radar transmits pulses of energy that illuminates the terrain. It then records the response returned from the objects or targets on the terrain towards the sensor (Lewis and Henderson, 1998). In a radar system, a transmitter sends out an amplified pulse of energy (a signal). When the pulse is received back (called an echo) after being reflected from the targets, it is amplified, converted to an intermediate frequency, detected and processed to generate the final radar product (Kingsley and Quegan, 1992).
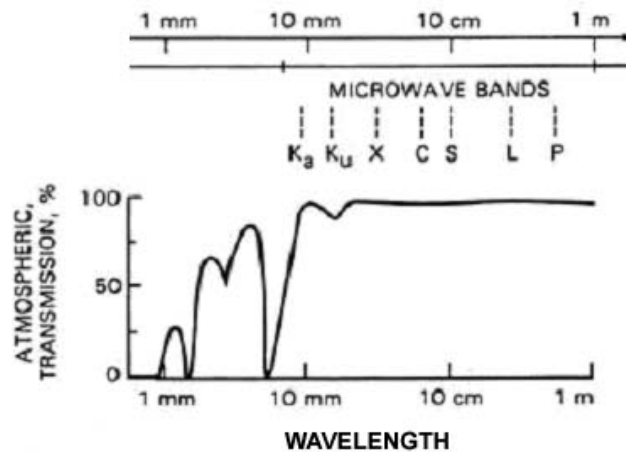
Figure 1-1 Electromagnetic spectrum showing atmospheric windows in the microwave regions (Lewis and Henderson, 1998)

The signal strength and time delay between transmission and reception are the main elements of the radar signal (Trevett, 1986). The main differences between the many imaging radars used in remote sensing are due to the antenna which determines the spatial resolution in the azimuth (or travel) direction (Raney, 1998). Imaging radars can be divided in two main categories, depending on the imaging technique used: Real Aperture Radar (RAR) also called Side Looking Airborne Radar (SLAR) and the Synthetic Aperture Radar (SAR). For both radar types the side-looking imaging geometry applies. The radar antenna illuminates a surface strip (footprint) to one side of the nadir track. The area continuously imaged from the radar beam is called the swath and can be divided into near range (the part nearer to the ground track) and far range. Each transmitted wave front hits the target surface at near range and sweeps across the swath to far range. The spatial resolution of a radar system can be defined as the minimum distance between two targets for them to produce separate backscatter or to be resolved as individual features (Lewis and Henderson, 1998). For imaging radars the spatial resolution is defined according to the flight direction. Azimuth spatial resolution is parallel to the flight direction and range spatial resolution is perpendicular to the flight direction.

The synthetic aperture imaging technique in a SAR uses the movement of the sensor to simulate a much larger antenna than its actual size. A single antenna moving along the flight line acquires the data and the effect is similar to using an array of antennas. The target is illuminated several times from different locations generating numerous echoes that are recorded coherently (i.e., amplitude and phase as a function of time) and subsequently combined to synthesize a linear array. A higher spatial resolution is achieved independently of the distance between sensor and target and by a small antenna (Elachi, 1988).

The Envisat satellite belonging to the European Space Agency is a polar-orbiting Earth observation satellite, carrying an Advanced Synthetic Aperture Radar (ASAR). The ASAR sensor has been designed not only to provide continuity to the ERS SAR, but also to extend the range of measurements through exploitation of its various operating modes. These modes enable varied capability in terms of swath width (58 to 405 km), range of incidence angles (from 14º to 45º), spatial resolution (30 to 1000 m) and polarization (HH, VV, VH and HV) (*Source: http://envisat.esa.int*)

1.2.2. System parameters

Interpreting radar data depends on an understanding of the interaction between system parameters and target characteristics. SAR systems have specific operational parameters which will influence the interaction between the pulses transmitted and the targets on the Earth's surface. System parameters are explained in the following sub-sections.

1.2.2.1. Wavelength

Most of imaging radars operate in a single band, defined either by its frequency (preferred by engineers) or wavelength (preferred by geoscientists) (Lewis and Henderson, 1998). The main reason for a single band operation is the limiting power supply, as radar systems rely upon their own energy source. Table 1.1 gives a description of the C band used for the present study

Table 1-1 Common wavelength/frequency bands for radar systems

Radar band	Wavelength – l(cm)	Frequency – f (MHz)
C	7.5-3.75	4000-8000

The interaction of microwaves and targets on Earth's land surface is dependent on the wavelength used. Penetration depth increases with the wavelength (Elachi, 1988). The roughness of a surface on a Radar image is also influenced by the wavelength used.

1.2.2.2. Polarization

Most of the radar systems use linear polarization, operating using vertically or horizontally polarized microwave radiation. As the microwaves are transmitted and received, the polarization is defined for the outgoing and incoming radiation and the antenna design must account for that. The linear polarization options commonly used are of two types viz. 1) Like polarized, horizontal transmit, horizontal receive i.e (HH) and vertical transmit, vertical receive i.e. (VV) 2) Cross polarized, Vertical transmit; Horizontal receive i.e. (VH) and Horizontal transmit; Vertical receive i.e. (HV). Targets on the Earth's surface scatter microwave radiation differently depending on the polarization of the wave transmitted. If the plane of polarization of the transmitted wave is parallel to the main line of polarization of the target being sensed the like polarized backscatter is stronger. For instance, a wheat field has a dominant vertical component, so the interaction and backscatter with a VV polarized wave is much stronger than that with a HH wave (Lewis and Henderson, 1998). The cross-polarization or depolarization of the transmitted wave is also a function of the amount of multiple volumetric scattering taking place at the targets. SAR systems with cross-polarized receiving capabilities can provide additional information for the image interpretation and understanding the target/wave interaction (Lewis and Henderson, 1998).

1.2.2.3. Incident angle

The incident angle (α) is a major factor influencing the radar backscatter and the appearance of the targets in the images. The incidence angle is the angle defined by the incident radar beam and the vertical (normal) to the intercepting surface. Figure 1.2 illustrates the system and local incident angles. In case of a flat surface, α is the complement of the depression angle (γ) (Jensen, 2000).
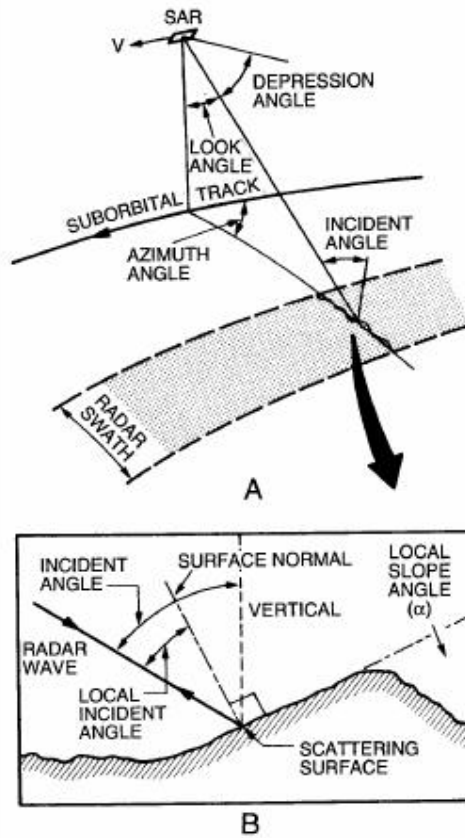
Figure 1-2 Schematic diagrams of (A) system and (B) local incident angles (Lewis and Henderson, 1998).

In general, smaller α results in stronger backscatter, although for very rough surfaces the backscatter is independent of α. Measured surface roughness changes as a function of the local incident angle (Lewis and Henderson, 1998). This parameter can be used to emphasize the roughness of particular features on the Earth's surface.

1.2.3.   Target characteristics

Radar backscatter is the result of the interaction between system parameters and the characteristics of the target, such as geometry (and associated roughness) and moisture content (and associated dielectric constant). First the backscattering coefficient is introduced, as it is a quantitative measure of backscatter intensity from a specific region on the Earth's land surface. Surface roughness and electrical characteristics of the targets are examined next.

1.2.3.1.   Backscatter coefficient

The targets scatter the energy transmitted by the radar in all directions. The energy scattered in the backward direction is what the radar records. The intensity of each pixel in a radar image is proportional to the ratio between the density of energy scattered and the density of energy transmitted from the targets in the Earth's land surface (Waring et al., 1995). The energy backscattered is related to a variable and is referred to as radar cross-section (σ), and is the amount of transmitted power absorbed and reflected by the target. The backscatter coefficient (σ °) is the amount of radar cross-section per unit area (A) on the ground (Jensen, 2000). σ ° is a characteristic of the scattering behaviour of all targets within a pixel. It varies over several orders of magnitude, and is a function of

wavelength, polarization and incidence angle, as well as target characteristics such as roughness, geometry and dielectric constants expressed as a logarithm with decibel units (Waring et al., 1995). The targets will be distinguishable in radar images if their backscatter components are different and the radar spatial resolution is adequate to discriminate between targets (Trevett, 1986).

1.2.3.2. Surface roughness

Surface roughness is one of the important target characteristics that influences the strength of backscatter and must be considered in relation to the scale at which the target is being observed. Three scales are often described: microscale roughness, mesoscale roughness and macroscale roughness, associated respectively with image tone, image texture and topographic effects (Lewis and Henderson, 1998).

Microscale roughness refers to the scale of small components (targets) within an individual pixel such as leaves and branches of trees or stones. Microscale is measured in centimetres and is a function of wavelength, the depression angle and the height of target or component of target. The modified Rayleigh criteria can be used to express this relationship (Jensen, 2000):

$$h < \lambda \, / \, 25 \, \mathrm{Sin} \, \gamma \qquad \qquad [1.1]$$

Where h is the local height of target or component of target, λ is the wavelength in cm and γ is the depression angle in degrees. Computing h using this criteria for $\lambda = 5.33$ cm (C band) and $\gamma = 45°$, results in $h < 0.30$ cm. If the local height of target is < 0.30 cm the target's surface is considered smooth and a near-perfect specular reflector. Therefore it will produce a dark tone in the image as no radiation will be backscattered to the sensor. Owing to intrinsic variations of depression angle from far range to near range, the image tone will also vary across the image (Lewis and Henderson, 1998). Mesoscale surface roughness is related to image texture and is a function of the characteristics of numerous pixels covering a single target, for instance, an entire forest canopy. With the same λ and γ, a forest canopy will present a coarser roughness (texture) than a grassland (Jensen, 2000). Macroscale surface roughness is influenced by shadow caused by topographic slope and the aspect of the terrain. The macro-texture patterns created by shadows are often many times larger than an individual pixel (Lewis and Henderson, 1998). Particular types of strong scattering occur when two or three smooth surfaces are adjacent, causing double or triple reflection. In this case the surfaces are known as dihedral or trihedral corner reflectors (Trevett, 1986).

1.2.3.3. Electrical characteristics

The electrical characteristics of targets also determine the intensity of backscatter. The complex dielectric constant is a measure of the electrical characteristics of objects, indicating the reflectivity and conductivity of various materials (Lillesand and Kiefer, 2000). The moisture content within materials has a direct influence on the dielectric constant and reflectivity. The more liquid water within a material the more reflectivity/backscatter is produced (Waring et al., 1995). Most materials have a dielectric constant ranging from 3 to 8 when dry, while water has a dielectric constant of around 80. Forest canopies are excellent reflectors because of the high moisture content in leaves, while dry soils absorb the radar signal and produce very low (or no) backscatter (Jensen, 2000).

1.3. Problem Statement

Excluding soil moisture and soil roughness other variables like incidence angle, polarization and wavelength also affect the radar backscatter signals. In order to extract reliable information on soil surface roughness from radar imagery, it is necessary to understand the degree to which these variables affect the radar signal. Previous studies carried out by (Baghdadi et al., 2002) have shown

that there is a strong influence of incidence angle on the discrimination between radar return over areas of different surface roughness. According to this study, at a higher incidence angle of 47^0, the influence of surface roughness on radar return predominates over the influence of other soil parameters, making it possible to discriminate and map various surface roughness classes. That study was carried out in a relatively flat study area using ERS and RadarSat data. (Fung and Chen, 1992) has shown that HH polarization is more sensitive to soil roughness than VV at high incidence angles. For determining surface roughness, a depolarized linear (e.g., HV) echo provides the largest dynamic range with RMS height, and avoids the complication of facet-like returns that contribute to polarized (HH or VV) echoes(Campbell and Shepard, 1996). (Baghdadi et al., 2002) concluded that at higher incidence angles the effects of soil moisture on radar response is less than that of soil surface roughness. Radar backscatter is affected by different surface properties over a range of local incidence angles. For local incidence angles of 0^0 to 30^0, radar backscatter is dominated by topographic slope and for angles of 30^0 to 70^0, surface roughness dominates (Lillesand and Kiefer, 2000). Most of the study till date has been an attempt to estimate surface roughness from radar backscatter done mostly in flat areas. As explained under the section on radar fundamentals, in relatively flat areas the angle of depression of the radar beam is equivalent or the complement of the local incidence angle. But in case of sloping terrain or hilly terrain the local incidence angle is likely to differ from the angle of depression of the radar beam. Also not much study has been done with regard to utility of ENVISAT –1 ASAR imagery with regard to surface roughness estimation for sloping terrain. This study proposes to investigate the effects of variables like local incidence angles, polarizations and soil moisture on ASAR backscatter in a sloping terrain, and to define the optimal configuration of ENVISAT-1 for the retrieval of surface roughness parameters. Envisat ASAR data is used for this study because it can do repeat measurements with a minimum duration of 5 days between two successive images at different incidence angles ranging from 15° to 45.2^o, as compared to 35 days for ERS and SAR. ENVISAT ASAR operating with 5.33 GHz bandwidth facilitates the acquisition of images with the option of selection of two simultaneous polarizations from the four polarizations HH, HV, VH, and VV.

1.4.   Objectives

The main Objective of the study is to establish the optimal configuration of local incidence angle and polarization for surface roughness estimation in ENVISAT-1 ASAR data. The following sub-objectives are identified to achieve the main objective

Sub-objectives:

- To study the influence of local incidence angles on the backscattering coefficient in sloping terrain.
- To study the influence of polarization configurations like HH, HV and VV on ASAR backscattering coefficient in sloping terrain.
- To study the influence of surface roughness on backscattering coefficients in slopping terrain.
- To study the influence of soil moisture on backscattering coefficients in slopping terrain.

1.5.   Research Questions

1) Is there a correlation between lower incidence angle and backscattering coefficient of ASAR data in sloping terrain?

2) Is there a correlation between VV polarization and backscattering coefficient of ASAR data in sloping terrain?

3) What is the optimal combination of local incidence angle and polarization for surface roughness estimation in ENVISAT-1 ASAR data?

1.6.   Thesis outline

In chapter 1 the rationale behind the research and basic information that underpins the five objectives are covered. Also Chapter 1 presents a review of radar fundamentals and the application of radar data for the study of surface roughness studies, establishing the theoretical framework for the research. Chapter 2 presents a review of the work done till date in surface roughness studies using radar data. It outlines the research work carried out till date and the recent trends in the estimation of surface roughness using SAR and ASAR data. Chapter 3 describes the study areas along with general information about Uttranchal the state in which the Sitla Rao water shed (study area) lies. Chapter 4 describes in detail the data used in the present study as well as the methods followed to achieve the objectives of the research project. Chapter 5 gives the results obtained by the application of the different methods described in chapter 4 and also discusses these research findings in detail. The conclusions for this research are drawn in Chapter 6 along with the recommendations for future research direction and need. Finally chapter 7 contains a bibliography of the references cited in the thesis report.

2. Review of Literature

A through understanding of the sensitivity of radar backscattering to surface parameters is crucial in developing inversion algorithms for microwave remote sensing. Soil moisture and surface roughness are significant indicators for hydrologic studies and the monitoring of agricultural environments. These parameters play an important role in the distribution of precipitation between runoff and infiltration. Extensive studies have been conducted on agricultural fields to assess the behaviour of radar signals as a function of soil moisture and surface roughness in the case of bare soil. The possibility of retrieving these soil parameters has been investigated by using scatterometers, satellites, space shuttles, and airborne synthetic aperture radars. The launch of the new European Environmental Satellite (ENVISAT) in March 2002, carrying the C-band Advanced Synthetic Aperture Radar (ASAR), should enable the scientific community to improve and increase its ability to retrieve physical parameters, based on ENVISAT's capability of providing images in HH, HV, and VV polarizations (two polarizations are possible simultaneously) and at various incidence angles between 150 and 450 (Baghdadi et al., 2006).

2.1. Influence of Surface parameters on radar Backscatter.

A study carried out in a flat 80-km2 Agricultural area to analyze the backscatter variability due to surface roughness concludes that multiple geometry of agricultural surfaces have a pronounced effect on radar backscatter. The authors found that the backscatter is influenced by the random surface roughness and is never smaller than 2 db. Also, the influence of the row pattern can be as strong as 10 db. The study concludes that the overall surface geometric effects depend upon several parameters including the incidence angle, look angle and the various roughness parameters like row direction random roughness and drainage relief. For ERS-1 and RADARSAT, the maximum effect of roughness was found with an incidence angle of 200, which decreases with an increase in the incidence angle up to 500, because, the effect of row structure and drainage pattern become negligible with increasing angle. (Beaudoin et al., 1990)

In a previous study polarimetric radar measurements were conducted for bare soil surfaces, under a variety of roughness and moisture conditions at L-, C-, and X-band frequencies at incidence angles ranging from 10-degrees to 70-degrees. Using a laser profiler and dielectric probes, a complete set of ground truth data were collected for each surface condition, from which measurements were made of the RMS height, correlation length, and dielectric constant. Based on knowledge of the scattering behaviour in limiting cases and the experimental observations, an empirical model was developed for σ_{hh}^{o}, σ_{vv}^{o}, and σ_{hv}^{o} in terms of ks (where $k = 2\pi / \lambda$ is the wave number and s is the RMS height) and the relative dielectric constant of the soil surface. The model, which was found to yield very good agreement with the backscattering measurements of this study as well as with measurements reported in other investigations, was used to develop an inversion technique for predicting the RMS height of the surface and its moisture content from multipolarized radar observations. The author concluded that at microwave frequencies the available rough surface scattering models are incapable of predicting the

scattering behaviour observed for bare-soil surface. He also observed that the co-polarized ratio p= $\sigma^o_{hh}/\sigma^o_{vv}$ $\leq$ 1 for all angles, roughness conditions and moisture contents p increases rapidly with increasing ks up to $ks \simeq 1$, then it increases at a slower rate, reaching the value 1 for $ks > 3$. For $ks < 3$, p deceases with increasing incidence angle and with increasing moisture content. He found that the

cross-polarization ratio q= $\sigma^o_{hv}/\sigma^o_{vv}$ exhibits a strong dependence on ks and a relatively weak dependence on moisture content. The ratio q increase rapidly with increasing ks up to $ks \leq 1$, then it increases at a slower rate, reaching a constant value depending upon the moisture content for $ks > 3$. (Oh et al., 1992)

(Hoeben et al., 1997) concluded that the roughness as seen by the radar can be expressed in terms of $k\sigma\cos\theta$ and $kL\sin\theta$. Where k is the free space wave number i.e. $\dfrac{2\pi}{\lambda}$ (λ = wavelength), σ is the surface RMS height, L is the surface correlation length and θ is the incidence angle. Since roughness parameters have an influence at smaller numerical values the knowledge about the correlation length L is important at lower incidence angles, while the RMS height σ has to be accurately known at higher incidence angles. The sensitivity of backscattering to the surface dielectric constant was found to decrease as the soil becomes wetter but is independent of other parameters such as radar configuration or roughness characteristics.

In a study conducted by (SU and Troch, 1997) on retrieval of bare surface soil moisture using data from the European Multisensor Airborne Campaign/ Experimental Synthetic Aperture Radar (EMAC/ESAR) the author concluded that conventional measurements of roughness are not accurate and such parameters introduce large errors in the predicted backscattering coefficients and hence in soil moisture retrieval. Such parameters cannot be blindly used in theoretical models such as IEM. The author proposed a method of `effective roughness parameters', using which the retrieved soil moisture accuracy is better than 5 per cent by volume. At least two independent radar observations are needed to retrieve soil moisture using active microwave data. The author further concluded that extensive study is needed with regard to the accuracy of field roughness measurements.

Analysis of semi-empirical models by comparison of the expected and measured backscattering values showed a better agreement for C-band HH polarization than for L- band. In spite of this agreement the main reason for errors in estimation could be the inaccuracies in the soil moisture and roughness measurements or due to the calibration errors of the data. Based on the research findings the author concluded that further refinement in modeling parameters needs to be done in case of catchment areas where relief (introduced by the local incidence angle) and vegetation coverage (introduced by the polarization ratio σ0hh /σ0vv) play a dominant role. (Neusch and Sties, 1999)

A study was conducted to explore the use of ERS-2 synthetic aperture radar (SAR) data to assess the soil water-content of agricultural farmlands. Field measurements of volumetric and gravimetric soil water-content and surface roughness were conducted, concurrent with the deployment of well-measured corner reflectors in the field for calibration and geo-rectification of the radar data. Results showed that where surface roughness was homogeneous, the radar backscatter cross-section correlated well with the soil water-content component. Also according to the author, while mapping water-content over several fields, the surface roughness must be incorporated into any model that correlates

radar backscatter with soil water-content. To develop a solution for roughness and soil water-content, the author acquired two ERS images with different look directions to get two different radar signatures. The derived empirical model to assess water-content conditions, explaining ca. 90% of the backscatter variation using water-content, roughness, and incidence angle. The authors concluded that since the model was empirical, it would not be universally true and therefore, the approach should be tested elsewhere.(Blumberg and Freilikher, 2001)

Previous studies have been carried to find out the potential of synthetic aperture radar (SAR) data for monitoring roughness states over bare agricultural fields on low-relief plateau with homogenous soil texture. The study was conducted using one ERS image (230) and two Radarsat images (390 and 470). The relationships between the backscattering coefficient, incidence angle, soil surface roughness and row direction were examined so as to determine the best SAR configuration for such monitoring. The results indicated a strong dependence of incidence angle on the discrimination between radar return over areas of different surface roughness. At a high incidence angle (470), the influence of soil roughness on radar return predominated over the influence of other soil parameters, making it possible to discriminate and map various surface roughness classes (smooth, medium and rough) over agricultural fields. However the author has also observed from the behaviour of the radar signals that ERS cannot be used for monitoring roughness states because the difference in σ^o between the various roughness classes is insufficient.(Baghdadi et al., 2002)

(Holah et al., 2005) carried out an investigation to analyze the sensitivity of ASAR (Advanced Synthetic Aperture Radar) data to soil surface parameters (surface roughness and soil moisture) over bare fields, which were considered as relatively, flat, at various polarizations (HH, HV, and VV) and incidence angles (200-430). The relationships between backscattering coefficients and soil parameters were examined by means of 16 ASAR images and several field campaigns. It was found that HH and HV polarizations are more sensitive than VV polarization to Surface roughness. The results also showed that the radar signal was more sensitive to surface roughness at high incidence angle (430). However, the dynamics of the radar signal as a function of soil roughness were weak for root mean square (RMS) surface heights between 0.5 cm and 3.50 cm. The estimation of soil moisture was found to be optimal at low and medium incidence angles (200- 370). The backscattering coefficient was more sensitive to volumetric soil moisture in HH polarization than in HV polarization. The results showed that the depolarization ratio σ0hh /σ0hv is weakly dependent on the roughness condition, whatever the radar incidence. While, a linear relationship was observed between the ratio σ0hh /σ0hv and the soil moisture. The backscattering coefficient ratio between a low and a high incidence angle decreased with the RMS surface height, and minimized the effect of the soil moisture. The author has also concluded that the ratios HH low-incidence / HH high-incidence and HV low-incidence / HV high-incidence are independent of the soil moisture. These conclusions were found to be in accordance to previous work done.

In another study carried out by (Baghdadi et al., 2006), the potential of Advanced Synthetic Aperture Radar (ASAR) for the retrieval of surface soil moisture over bare soils was evaluated for several ASAR acquisition configurations: (1) one date/single channel (one incidence and one polarization); (2) one date/two channels (one incidence and two polarizations); (3) two dates/ two channels (two incidences and one polarization); and (4) two dates/four channels (two incidences and two polarizations). It was found that when compared with the results obtained with a single polarization

(HH or HV), the use of two polarizations (HH and HV) does not enable a significant improvement in estimating soil moisture. For the best estimates of soil moisture, ASAR data should be acquired at both low and high incidence angles. ASAR proves to be a good remote sensing tool for measuring surface soil moisture, with accuracy for the retrieved soil moisture that can reach 3.5% (RMSE).

Similar studies have got to be conducted to estimate the potential of ASAR for retrieval of surface roughness.

2.2. Surface roughness field measurements

The surface roughness is usually characterized by an RMS surface height (RMS), which specifies the vertical scale of the roughness, and by a surface autocorrelation function with the characteristic correlation length (l), representing the horizontal scale. The surface correlation length is usually defined as the displacement x for which the autocorrelation function $f(x)$ of the profile is equal to 1/e.

Simulation studies were conducted in Monte Carlo to find the optimum length and sampling interval of the surface height profile. Results indicated that in order to measure the RMS height and the correlation length with a precision of +/-10%, the surface segment should be at least 40 l long and 200 l long, respectively, where l is the mean (or true) value of the surface correlation length. Shorter segment lengths can be used if multiple segments are measured and then the estimated values are averaged. The second part of the study focused on the relationship between sampling interval and measurement precision. It was found that, in order to estimate the surface roughness parameters with a precision of +/-5%, it is necessary that the surface be sampled at a spacing no longer than 0.2 of the correlation length. Based on these simulations the authors showed that the correlation length measurements are unreliable and inaccurate when conventional profilometers of 1 to 2 meters long are used. (Oh and Kay, 1998)

The input roughness parameters for electromagnetic backscattering modelling need to be accurate to estimate radar measurements correctly over bare soils, particularly in agricultural environments. A study was carried out to evaluate the roughness description in terms of several characterizations through a correlation function using a numerical backscattering model. The experimental database used in this study was based on ASAR-ENVISAT experimental campaigns in the Beauce region (France). Two presentations of the surface height correlation function are proposed in this study. The first one, referred to as the "alpha function" fits the experimental correlation functions up to the correlation length, while the second one, the "(a, b) function", fits the correlation function for scales corresponding to positive values. A relationship was proposed between the RMS height of soil surface and the shape of the correlation function. The use of the alpha function, for comparisons between radar measurements for high incidence angles and simulations based on the numerical backscattering model (moment method) showed a good agreement for soil surfaces with an RMS height smaller than 2 cm with medium and high soil moisture. (Zribi et al., 2005)

2.3. SAR Image Processing

Due to the side looking geometry of SAR-systems undulated terrain is significantly distorted during the SAR mapping process. The most important and well-known local image distortions are foreshortening, layover, and shadow. But also the range displacement effect needs to be considered that causes elevated features to be mapped in false range positions – namely to closely to near range.

These effects as well as the varying ground resolution caused by varying slopes can be corrected using a digital elevation model. All ASAR Level 1-b image products produced from the Level 0 data (besides IMG and APG) can serve as input for the Geocoding System. The principle of this approach is to perform the rigorous transformation for grid points and using an interpolation to fill the grid cells. The radar image range and time co-ordinates are determined by interpolating between anchor points. At first a three-dimensional grid of points (co-ordinates in easting, northing, height) is generated and the corresponding pixel co-ordinates (in azimuth and range) of the input image are determined using the rigorous Range-Doppler approach. The grid covers the output area and its height extension spans the entire elevation range of the underlying DEM. Starting from the azimuth and range co-ordinates at a reference elevation correction terms in azimuth and range are interpolated using the individual height values from the DEM. (Martin et al., 2005)

A study conducted by (Small et al., 2004) concluded that for ground range ASAR products (image mode IMP & IMM, alternating polarization APP & APM, or wide swath WSM), the AGP is modelled using an Earth ellipsoid assumption and compensation applied before image generation. If more rigorous terrain-dependent AGP compensation is desired, then the ellipsoid-based compensation must first be reversed before a terrain-based model may be applied. The author concluded that radiometric refinements by terrain-dependent AGP correction gave best results for the steepest antenna gain patterns (IS1, IS7)

2.4.   Dem Generation

The ASTER Level-1B data are L1A data (i.e. raw data reconstructed from Level-0, and are unprocessed instrument digital counts) with the radiometric and geometric coefficients applied. The L1B image is projected onto a rotated map (rotated to "path oriented" coordinate) at full instrument resolutions. The Level-1B data generation also includes registration of the SWIR and TIR data to the VNIR data. And in addition, for SWIR in particular, the parallax errors due to the spatial locations of all of its bands are corrected. Level-1B data define a scene centre as the geodetic centre of the scene obtained from the L1A attribute named "SceneCenter" in the HDF-EOS attribute "productmetadata.0". The definition of scene centre in L1B is the actual centre on the rotated coordinates (L1B coordinates) not the same as in L1A (*Aster (Handbook), ver2*)

The Advanced Space borne Thermal Emission and Reflection Radiometer (ASTER) provides along-track digital stereo image data at 15-m resolution. A study was conducted to evaluate the accuracy of the ASTER digital elevation model (DEM), stereo image data for which four study sites around the world were employed to validate prelaunch estimates of height accuracy. Automated stereo correlation procedures were implemented using the Desktop Mapping System (DMS) software to derive DEMs with 30- to 150-m postings. Results indicate that a root-mean-square error (RMSE) in elevation between +/-7 and +/-15 m can be achieved with ASTER stereo image data of good quality. An evaluation of an ASTER DEM data product produced at the US Geological Survey (USGS) EROS Data Centre (EDC) yielded an RMSE of +/-8.6 m. *(Hirano et al., 2003)* similar results were also observed by (Ping, 2003)

A study to evaluate the accuracy of DEMs extracted from ASTER data was conducted on two test sites in Switzerland, which were well documented. The DEMs were generated with the software package PCI Geomatica V.8.0. The accuracy was tested by comparing the DEMs before and after

post-processing to two reference models: First a high accuracy surface model generated with InSAR technology and second to the DHM25, an elevation model based on digitized contour lines of the 1:25000 topographical maps. The selected test sites are situated in the Swiss Alps. They are characterized by high relief with an elevation range of up to 2000 m. In the post-processing step noise removal and interpolation of missing data was performed. A gaussian smoothing filter was applied twice. Although refinement could be achieved where data was missing, big blunders in the forested areas and on steep, rocky cliffs could not be avoided. In spite of these limitations the accuracy of the generated DEMs was found to be promising, considering the extreme terrain. An RMSE of 20.52 m and 28.80 m respectively was achieved for the two test sites. The results of the comparisons with the two reference models show that the DEMs are reliable in flat regions and on slopes. *(Eckert and Kellenberger, 2002)*

3. Study Area Description

The Garhwal (west) and Kumaon (east) form the mountainous state of Uttaranchal. The state Uttaranchal contains a large part of the Indian Himalayas. It is bordered to the north by Tibet and to the east by Nepal. On the west side it is bordered by the state Himachal Pradesh and on the south side by the state Uttar Pradesh. Before 2000 it was the mountainous part of the state Uttar Pradesh. Since November 2000 this part of Uttar Pradesh has become a separate state, Uttaranchal. The study area is located in the western part of the Doon valley in the Dehradun district of Uttranchal state. The main study was limited to the Sitlarao sub-watershed, which belongs to the Asan river system, which is a tributary of the river Yamuna.

3.1. Location

The main area selected for the study falls within the Sitlarao watershed, which is a part of the Dehradun district. The study area is delineated by the SOI toposheet No. 53 F/15 at 1: 50000 scale. The study area is located between latitude 30^0 25' N to 30^0 30' N and Longitude 77^0 45' E to 78^0 0' E. The location of the study area is presented in Figure 3.1
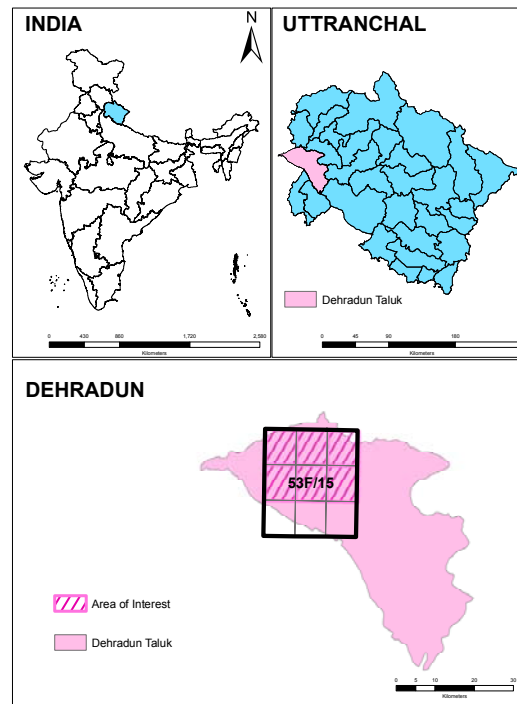
Figure 3-1 Area Of Interest

3.2. Climate

The climate is characterized by hot summers, which are humid to sub tropical varying from the Doon valley to the higher mountain ranges of the Himalayas and cold winters. The mean annual temperature ranges from 15.8^0 C in winter to 33.3^0 C in summer. The rainfall received is from June to August and varies from 1600 to 2200 mm, depending on the elevation of the area.

3.3.   Geology

The area is known for its complex lithology and forms a large part of the Siwalik side slope and alluvial plain. The area is characterized into mainly four types of geomorphic units, which are the upper Siwalik side slope, the middle Siwalik side slope, piedomont and alluvial plain. The characteristics features of the upper Siwalik are rocks, boulders, conglomerates and pebble conglomerate with sandy matrix, layers of sandy matrix and sand, which is mainly found in the lower portions of this formation. The upper portion is predominantly dissected by a number of sub parallel, non-perennial streams. The piedomont and the alluvial plains have been formed by the deposition from a number of rivulets and rivers. The main material comprising the piedmont zone is of coarser gravels and sandstones.

3.4.   Physiography

 Physiographically the area is divided into four major units based on similarity in relief, slope, texture, geology and arrangement of landform features, hill side slope, upper piedmont, middle piedmont and lower piedmont.

3.5.   Soils

The soils are mainly classified as Alfisols, entisols and inceptisols. The existing rainfall and temperature data shows that the area qualifies for the ustic soil moisture regime and the hyperthermic soil regime respectively. The soil texture varies from loamy to clay loam while the soil depth varies from being moderately deep to very deep

3.6.   Landuse / Land cover

The major landuse / land cover of the study area are forest, agriculture, scrub and settlements. The main cropping season is kharif and Rabi. Mostly paddy, maize and sugarcane are grown in the kharif season where as wheat is cultivated during the Rabi season.

3.7.   Drainage

 The study area is sloping down towards southwest from Pasta village. The runoff water from the river and streams of the sub watershed flow into the main river Sitlarao. The contributing streams are the guna, maruti and koti nadi.

3.8.   Socia-economic conditions

Agriculture is one of the most important and widespread occupations of the region with over 75% of the population involved in this activity. The people of the region follow a mixed farming system with animal husbandry and agriculture being the major two components. The economy of the region is predominantly agrarian. Other important occupations include horticulture, forestry and livestock farming.

4. MATERIALS AND METHODS

4.1. Data description

A brief description of the basic characteristics of the different datasets used is given below

4.1.1. ASAR (Advanced Synthetic Aperture Radar) data:

ENVISAT ASAR alternating polarization mode precision images (APP-1P) which are ground range corrected provided by the European Space Agency (ESA) are used for this study. ENVISAT ASAR provides images in a wide range of swaths from IS1 to IS7 with an incidence angle range from 15^0 to 45.2^0 . For this study based on availability, three swaths were selected to represent the range of incidence angles offered by ENVISAT ASAR sensor. A brief description of the characteristics of the selected swaths are provided in Table 4-1

Table 4-1 Specifications for ENVISAT ASAR image mode swaths used in the study

Image Swath	Swath Width (km)	Ground, position from nadir (km)	Incidence Angle Range	Worst Case Noise Equivalent Sigma Zero
IS2	105	242 - 347	19.2 - 26.7	-20.6
IS4	88	412 - 500	31.0 - 36.3	-19.4
IS6	70	550 - 620	39.1 - 42.8	-22.0

Source: (ESA, 2006)

ASAR APP-1P is a stand-alone multilook, ground range, narrow swath digital image generated using the SPECAN algorithm from the Level 0 data collected when the instrument is in the Alternating polarization mode. Generation of this product involves the use of a technique, which allows half of the looks of an image to be acquired in horizontal polarization and the other half in the vertical polarization. The product therefore contains two CO-registered images corresponding to one of the three polarization combination available (HH and VV, HH and HV, VV and VH). For this study only the HH and HV, VV and VH combinations are taken into consideration. This product has got a geometric resolution of approximately 30m-ground range and a pixel spacing of 12.5m x 12.5m in the range and azimuth direction respectively.

A brief description of the data acquired is shown in Table 4-2 and Table 4-3

Table 4-2 Description of ASAR data acquired during monsoon

Sl	Latitude	Longitude	Polarization	Acquisition date	Pass	Orbit	Track	Swath
1	30.5167 N	77.5667 E	HH/HV	05-Aug-2006 04:57:41	D	23162	62	I2
2	30.4333 N	77.9500 E	VV/VH	18-Aug-2006 04:49:10	D	23348	248	I4
3	30.3833 N	78.2667 E	VV/VH	21-Aug-2006 04:54:51	D	23391	291	I2
4	30.3500 N	77.5333 E	HH/HV	26-Aug-2006 16:48:37	A	23470	370	I4
5	30.4500 N	78.1667 E	HH/HV	10-Aug-2006 16:51:28	A	23241	141	I6
6	30.3500 N	77.4667 E	HH/HV	29-Aug-2006 16:54:18	A	23513	413	I6

Table 4-3 Description of ASAR data acquired after monsoons

Sl	Latitude	Longitude	Polarization	Acquisition date	Pass	Orbit	Track	Swath
1	30.3500 N	77.4667 E	VV/VH	03-Oct-2006 16:54:27	A	24014	413	I6
2	30.4500 N	78.1667 E	VV/VH	19-Oct-2006 16:51:38	A	24243	141	I6
3	30.4333 N	78.0167 E	HH/HV	24-Oct-2006 04:43:39	D	24307	205	I6
4	30.4667 N	78.2167 E	HH/HV	16-Oct-2006 16:45:56	A	24200	98	I4
5	30.3833 N	78.2667 E	VV/VH	25-Sep-2006 04:54:58	D	23892	291	I2

4.1.2. Description of ASTER stereo system and image for DEM generation

The ASTER "pushbroom" linear array sensor is designed to provide image data in 14 bands, which are three Visible and Near-infrared (VNIR) bands with 15 m spatial resolution, six Short-wave Infrared (SWIR) bands with 30 m spatial resolution, and five Thermal Infrared (TIR) bands with 90 m spatial resolution.

For DEM generation the stereo image data are recorded only in Band 3, which is the near-infrared wavelength region from 0.78 to 0.86 μm, using both nadir and aft looking telescopes. From an altitude of 705 km, the aster sensor covers a 60 km wide ground track at a 15 m spatial resolution. As shown in Figure. 1, there is an approximately 60 seconds interval between the time the nadir telescope passes over a ground location and the aft telescope records the same location on the ground track of the satellite. Images generated from the nadir and aft telescopes yield a base to height (B/H) ratio of 0.6. One of the advantages of the aster sensor data is that the sensor operates in an along-track mode of data acquisition therefore the resulting images forming the stereo pairs are acquired in a few seconds (rather than days) apart under uniform environmental and lighting conditions, resulting in stereo pairs of consistent quality that are well suited for DEM generation. These characteristics of the aster data make it ideal for generating DEMs by automated techniques for different terrain conditions. (Hirano et al., 2003)

The data used in the present study for the generation of a DEM are L1B (radiance) data with geometric and radiometric correction. The aster stereo image with granule id AST_L1B_003021020003054307

was acquired on 2nd October 2003 at 5 hrs 43 min and 07 sec and has zero percent cloud cover. The data was purchased via the ITC RSG laboratory.

4.1.3. Ancillary data Used

DEM generated from 20 m interval contours *(source IIRS -Dehradun)*. Source toposheet index number 53F/15 at 1:50000 scale.

4.1.4. Landsat-7 ETM+ orthorectified Pan image

The Landsat 7 satellite was launched from Vandenburg Air Force Base on April 15, 1999. Its payload is a single nadir-pointing instrument, the Enhanced Thematic Mapper Plus (ETM+). A brief description of the ETM+ Orthorectified Panchromatic band characteristics is shown in Table 4-4. In the present study this data is used as an additional source for georeferencing of ENVISAT ASAR data. This data was downloaded from the site *http://glcfapp.umiacs.umd.edu:8080/esdi/index.jsp*.

Table 4-4 Landsat-7 ETM pan band characteristics

Platform	Landsat7
Sensor id	ETM+
Acquisition date	11/25/2000
Path number	146
Row number	39
Scene center latitude	30.309 N
Scene center longitude	78.276 E
Map projection	UTM
Zone number	44
Reference datum	WGS84
Reference ellipsoid	WGS84
Band number	8
Wavelength	0.52-0.90 (μm)
Grid cell size	14.250 m
Sun azimuth	155.55 deg
Sun elevation	34.94 deg

4.1.5. Field data / samples description

The present study requires the collection of a various types of data from the field. The various data collected in the field are listed below in table 4-5 along with its intended use.

Table 4-5 Description of Field data / samples and intended use

Field Observations	Purpose
GPS point locations	Identification of sampling points as well as locations for installation of Corner Reflectors
Soil Surface roughness	Root Mean Square (RMS) Height calculations
Crop height	Surface roughness indicator
Soil samples	Analysis for volumetric soil moisture, pH, Bulk density
Ground Control Points (GCPs)	Generation of DEM from stereo pair data

A detailed description of the methods used to collect the field data / samples as well as the different processing techniques used to generate the Digital Elevation models and process the satellite data sets, to achieve the objective of this study is given in section 4.2.

4.1.6. Instruments used for data collection

Table 4-6 gives a brief overview of the different instruments used for data collection along with their purpose

Table 4-6 Overview of Instruments used and their purpose

Instrument	Purpose
ArcPad 6.0.3 based Mobile GPS mounted on palm top	Identification and direction to sampling points as well as in field location of selected GCP points for DGPS survey
Leica GS-50 Differential Global Positioning System (DGPS)	Precise and accurate location of GCPs and corner reflector positions
Pin profilometer (1 meter long and needle spacing of 2 cms)	Surface roughness measurements (RMS Height)

4.2. Methods Used in this study

A detailed description of the methods implemented for field data collection and geo-data processing is given in the sections to follow

4.2.1. Field data collection and analysis

The present study required real time field data collection at the time of satellite data acquisition. Various data like soil moisture, soil pH, crop height, crop type and surface roughness states were collected at the time of the satellite data acquisition to give an idea of the real time conditions of the surface characteristics at the time of ASAR data acquisition. This data was collected on the same day

+/- 2 hours the duration of the ENVISAT ASAR data acquisition time. The methods employed and the procedures followed to accomplish this requirement are described in the following subsections.

4.2.1.1. Sampling Strategy

Prior to data collection a random stratified sampling strategy was employed to decide on the location and number of the sampling points (comparatively large and homogenous agricultural fields) to be considered for the study. This was done taking into consideration the land cover classes, the local terrain elevation, the slope classes, the crop type, soil type and accessibility to the area keeping in mind the fact that the data collection would have to be done in a limited period of time. For this study the main land cover class taken into consideration is the agricultural areas. An existing land cover map (*source IIRS*) was used to extract the agricultural area in the study area. A slope map was generated from the DEM and five slope classes were defined as $0\text{-}5^0$, $5\text{-}10^0$, $10\text{-}15^0$, $15\text{-}20^0$ and greater than 20^0. The basic criterion for selecting the slope classes was to evaluate the effect of increasing slope (degrees) on the backscattering coefficient in ASAR data. A field survey was then undertaken to select the sampling points. Based on the criteria mentioned above 21 sampling points were selected in the study area. The locations of all the selected sampling points were then recorded using ArcPad to facilitate revisits to the same selected agricultural fields for subsequent data collection. The sampling for each point was done during monsoon and after monsoons to take into account the variation due to moisture contents. Figure 4-1 gives an overview of the location and distribution of the sampling points selected for the study. Table 4-7 gives the characteristics of the sampling points selected for the study.
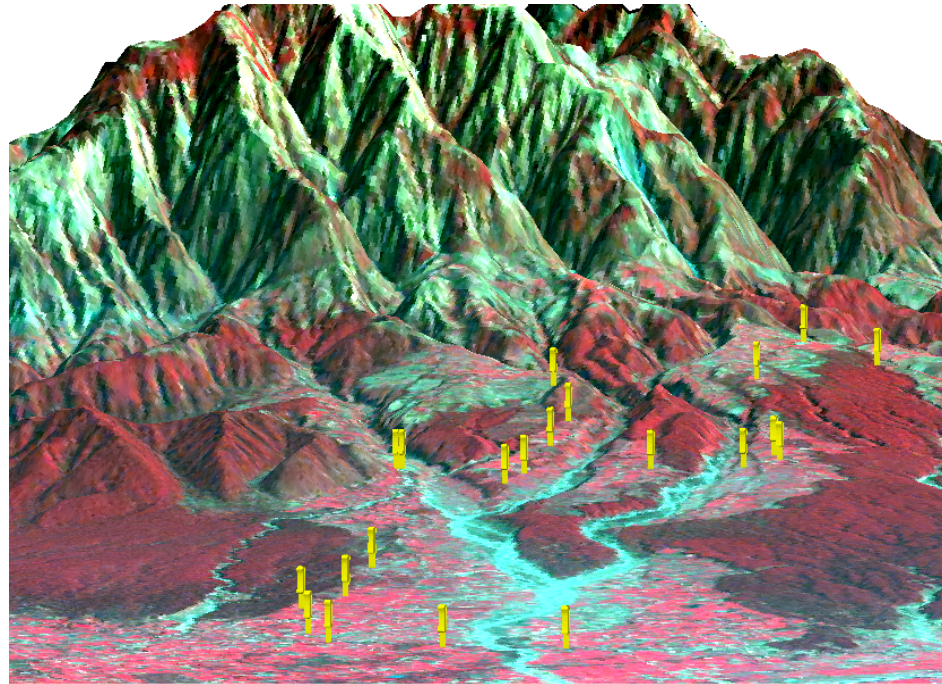
Figure 4-1 Overview of sample points selected for the study draped over Aster level-5 DEM

Table 4-7 Description of the Sampling Points selected for this study

Point-ID	Crop Type	Slope Class (degrees)	Description	Soil Classification
1	Maize	15-20	Deep, well drained, fine loamy soils on gentle slopes with loamy surface and slight erosion; *associated with:* Deep, well drained, fine loamy soils with loamy surface and slight erosion	*Fluventic Eutrochrepts* Associated Soils: *Typic Udifluvents*
2	Maize	0-5		
3	maize	15-20		
4	Sugarcane	10-15		
5	Maize	>20	Deep, well drained, fine loamy soils on gentle slopes with loamy surface and slight erosion; associated with: Deep, well drained, coarse loamy soils over fragmented soils with loamy surface and slight erosion	*Dystric Eutrochrepts* Associated Soils: *Fluventic Eutrochrepts*
6	Paddy	10-15		
7	maize	>20		
8	Maize	0-5		
9	maize	10-15		
10	paddy	>20		
11	paddy	15-20		
12	Cherry	15-20		
13	Maize	5-10		
14	paddy	>20		
15	maize	0-5		
16	paddy	15-20		
17	maize	15-20		
18	maize	15-20		
19	paddy	5-10		
20	maize	5-10		
21	paddy	15-20		

4.2.1.2.   Surface roughness measurements and calculations

Surface roughness measurements were done using a pin profilometer, one meter in length and having a sampling interval of 2cms *(Baghdadi et al., 2002)*. The roughness profiles were measured perpendicular to the row directions. For each sampling point three sets of roughness observations were taken and the RMS surface height was then calculated for each sample point using the following equation 4-1.*(Gupta and Kapoor, 2003)*

$$RMS_{height} = \sqrt{\frac{1}{n_1 + n_2 + n_3}\left[n_1\left(\sigma_1^2 + d_1^2\right) + n_2\left(\sigma_2^2 + d_2^2\right) + n_3\left(\sigma_3^2 + d_3^2\right)\right]} \quad \textbf{Equation 4-1}$$

Where, σ^2 is the variance calculated for each of the three surface roughness profiles as σ_1^2, σ_2^2 and σ_3^2 using equation 4-2

$$\sigma^2 = \frac{1}{n} \sum_{i=1}^{n} (x_i - \overline{x})^2$$ **Equation 4-2**

and $d_i^2 = (\overline{x}_i - \overline{X})^2$ where $\overline{x}_i$ is the mean calculated individually for each of the three sets of surface

roughness profiles (i.e. i = 1, 2, 3) and $\overline{X}$ is the total mean of all the three surface roughness profiles taken together calculated using equation 4-3

$$\overline{X} = \frac{n_1 \overline{x}_1 + n_2 \overline{x}_2 + n_3 \overline{x}_3}{n_1 + n_2 + n_3}$$ **Equation 4-3**

Where n_1, n_2 and n_3 are the total number of observation for profile 1, 2 and 3 respectively.

During the monsoon season as most of the fields were cultivated, the crop height was measured as an indicator for surface roughness. The measurements were taken for a one meter long profile with four sets of observations for each sampling point. The sampling interval was determined by the spacing between the crops. The RMS height was then calculated using the equation 4-4 (Blumberg and Freilikher, 2001)

$$RMS_{height} = s = \sqrt{\frac{\sum_{i=1}^{n} (z_i - \overline{z})^2}{n-1}}$$ **Equation 4-4**

z_i = crop height readings for all the observation sets from 1 to ….n

$\overline{z}$ = the mean crop height over all points from 1 to ….n

n = total number of observations

4.2.1.3.   Soil sample collection methods and sample analysis procedures

Soil sampling for all the sample points were carried out in accordance to standard soil sampling procedures. For each sampling point a composite of five soil samples were collected at two depths of 5cm and 10cm and processed for further analysis. The collected soil samples were then analyzed for volumetric soil moisture content (dried at 106^0 Celsius), soil pH and bulk density using the standard analytical procedures.

4.2.1.4.   Database creation

Point map of sample locations was generated. Database for the average RMS height, volumetric soil moisture content at 5cm and 10 cm depth, soil pH and Bulk density for each of the observation dates was created and then linked to the location map.

4.2.2.   DEM generation and validation

The present study required the generation of a precise DEM for the calculation of the local incidence angle image and derivation of the radar backscattering coefficients. For this purpose two DEMs were generated from available sources i.e. 20 meter interval contours and Aster Stereo image pair and the accuracy of both DEMs were validated. After the validation, DEM generated from aster stereo image pair was selected based on a lower RMS height error. The procedure followed for the generation of the DEMs and the method for the validation of the DEMs is described in the sections to follow

4.2.2.1.   GCP collection

For the purpose of generating a DEM from the aster stereo image pair it was necessary to conduct a DGPS survey to collect the required GCPs. Since the pixel spacing of the ASAR APP image is 12.5 meters in the azimuth and range direction, the required resolution of the output DEM was also fixed at 12.5 meters. The accuracy of the GCP points collected had to be less than the resolution of the output DEM. Since the GCPs were collected using DGPS equipment the accuracy of the points collected is expected to be considerably lower than the resolution of the output DEM.

Before conducting the DGPS survey an FCC of bands 3N (N = nadir, $\lambda = 0.8070\,\mu m$), band 2 ($\lambda = 0.6610\,\mu m$), band 1 ($\lambda = 0.5560\,\mu m$), was georeferenced using the ETM- orthorectified pan image. The GCP points required for the DGPS survey were then identified in this georeferenced image. The GCP points selected for the DGPS survey were mainly road intersections. An overview of the distribution of the selected points is shown in figure 4-2. A vector map of these points was then loaded in ArcPad along with the georeferenced aster image to facilitate easy identification of these points in the field. The reference site to establish a base station was chosen, such that there was no obstruction above a 15^{0} cut off angle. And also there were no reflecting surfaces or powerful transmitters in the vicinity. The reference site was located at Northing of "776404.5188" meters and Easting of "3372582.1829" meters in the UTM projection system.

When carrying out a DGPS survey a baseline is observed and computed between two receivers. When the two receivers observe the same set of satellites simultaneously, most of the atmospheric effects cancel out. The shorter the baseline is the more these effects will be reduced, as the more likely it is that the atmosphere through which the signals pass to the two receivers will be identical [*source: (LeicaGeosystems)*]. The selection of points was done so that the baseline distance between the reference and the rover was within 10 km range. Based on the recommendation that for 4 or more satellites having a GDOP (Geometric dilution of precision) <= 8 and a baseline length between 5-10 km the approximate observation time by day should be around 10- 20 min. [*source : (LeicaGeosystems)*] the observation time for each point during the survey was kept at 45 minutes each. This would help to resolve the ambiguity during the post processing of the collected GCP points. For recording the points the DGPS instrument was set with a GDOP = 5 and a cut off angle of 15^{0}. A total of 23 GCP points were collected in the field.
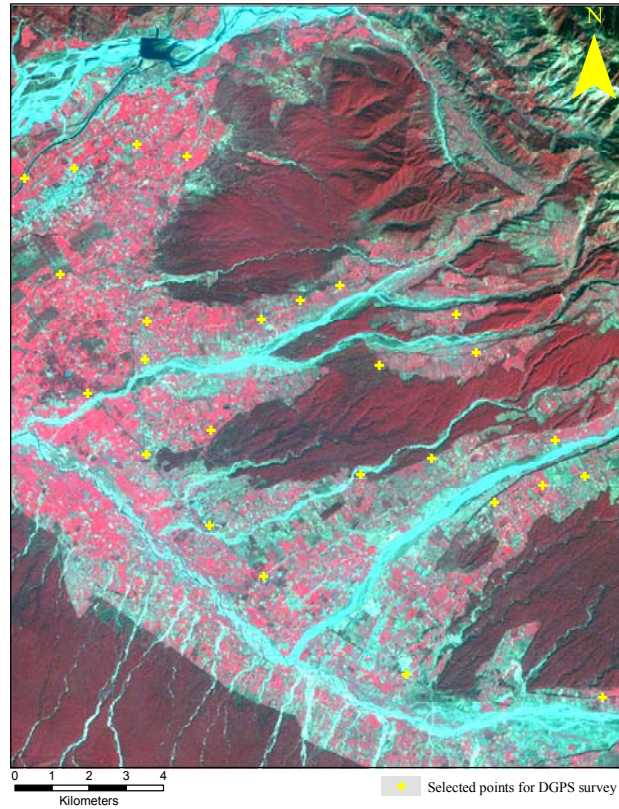
Figure 4-2 Distribution of Selected GCPs for DGPS survey

4.2.2.2. Post processing of collected GCPs

The post processing of collected GCP points was then done using the Leica Skipro® post processing software available at IIRS. During the post processing the positional quality for all collected points was improved. The input parameters used for the post processing of the GCP points are shown in Table 4-8

Table 4-8 Input parameter settings for Post-processing of GCP points

Parameters	Settings
Cut-off angle	15^0 - 20^0
Ephemeris type	Broadcast
Solution type (to resolve ambiguities)	Automatic
Frequency	L1
Fix Ambiguities up to	80Km
Minimum duration for float solution(static)	300 sec
Troposheric model	Hopfield
Ionospheric Model	Automatic
Stochastic Modeling	Yes
Minimum distance	8 km
Ionospheric activity	Automatic

The positional quality of the GCP points before and after post-processing are shown in Table I-A and Table I-B respectively in Appendix-I

4.2.2.3.   Aster stereo image processing for DEM generation and validation

The generation of an absolute DEM from aster stereo image pair was done using the DEM extraction module available in the topographic tools of the ENVI software. Of the 23 points that were post processed, 13 points were used for the generation of the DEM. Basically there were three steps involved in the extraction of the DEM explained below.

Epipolar Image Creation - Epipolar geometry describes the geometrical constraint between two frame images of a stereo pair. It represents the fact that a ground point and the two optical centres lie on the same plane. This means that for a given point in one image, its conjugate point in the other image must lie on a known line in the second image. By creating epipolar images, the search space for finding corresponding image points in automatic image matching is reduced. To generate the epipolar image, the left and right stereo image of the aster stereo image pair were first opened in the step one of the DEM extraction wizard. The RPC of the stereo image pair was computed and the minimum and maximum elevation values were automatically set from the RPCs. In the next step, the "Define GCPs Interactively" option was chosen. The 13 post processed GCPs were then manually entered and edited.

Figure 4-3 shows a snap shot of this step in the extraction wizard. After all the GCPs were entered, the generate tie point option was selected with the "examine and edit tie point" option enabled. A total of 50 tie points were generated and edited to ensure accuracy. After editing the tie points, a maximum Y-parallax of 0.4288 was achieved. Figure 4-4 shows a snap shot of the maximum parallax achieved
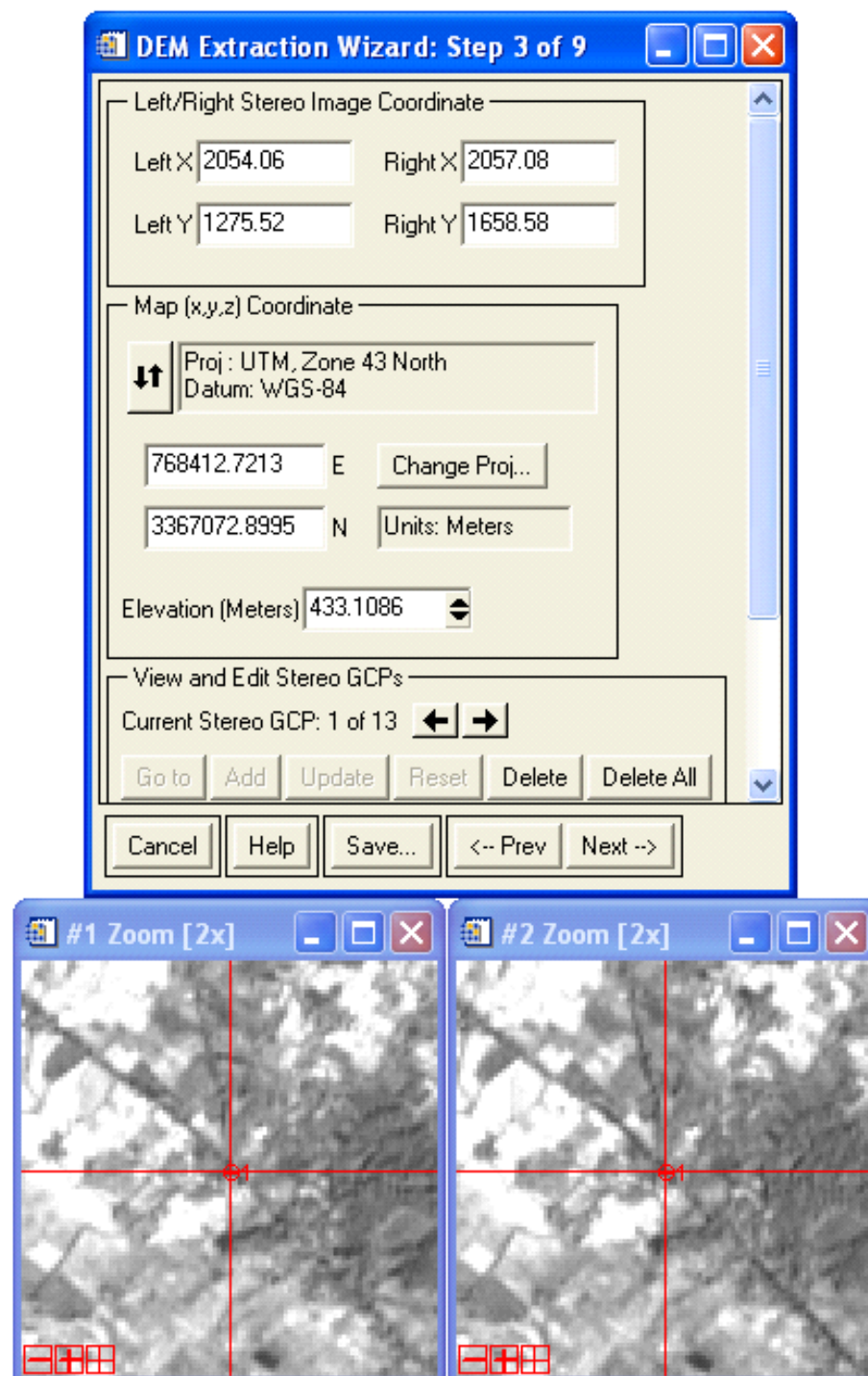
Figure 4-3 Snap shot of manually entered GCPs (step 3)
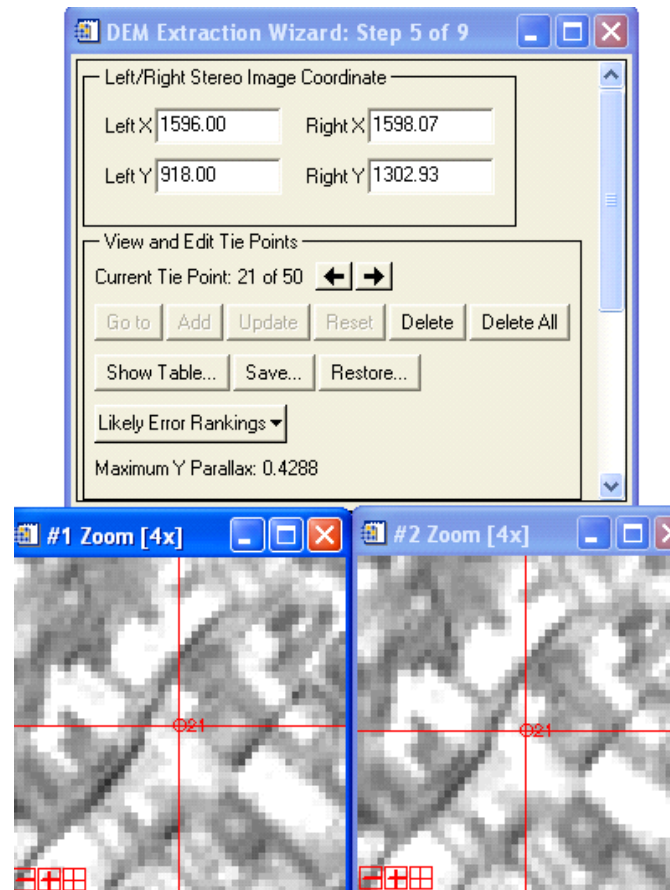
Figure 4-4 Snap shot of step 5 in the DEM generation process

The next step in the DEM extraction wizard generates the epipolar images. After which it performs an image matching process to find the conjugate points on both, the left and right images which correspond to the same ground feature. The output of the image matching procedure is called a parallax image, in which the x-coordinate difference (along epipolar lines) between the left and right image is stored and is used to build the DEM. Thus, the quality of image matching largely determines the quality of the output DEM. For the generation of the DEM, the output resolution (cell size) was given as 12.5 meters. This was to ensure that the ASAR image and the DEM would be in the same resolution. In the next step the DEM geocoding, which re-projects the DEM from the epipolar projection to the specified projection and map units, is performed. This step involves the filling of failed pixels and then resampling to the specified pixel spacing. Since GCPs are provided, the absolute orientation of the computed terrain model is performed in this step. By this process a level 5 aster DEM was generated.

After the generation of the DEM, a validation was performed using the remaining post processed GCP points. Seven points were used and the height information at these seven points was extracted from the generated Aster level-5 DEM. The RMSE of the heights was calculated between the observed heights at the seven points and the heights extracted from the DEM. The RMSE was found to be 8.45 meters which is the expected height accuracy of a DEM generated from stereo aster image pair according to previous studies. Figure 4-5 shows a snap shot of the Aster level-5 DEM generated draped with a georeferenced ASTER False colour composite image.
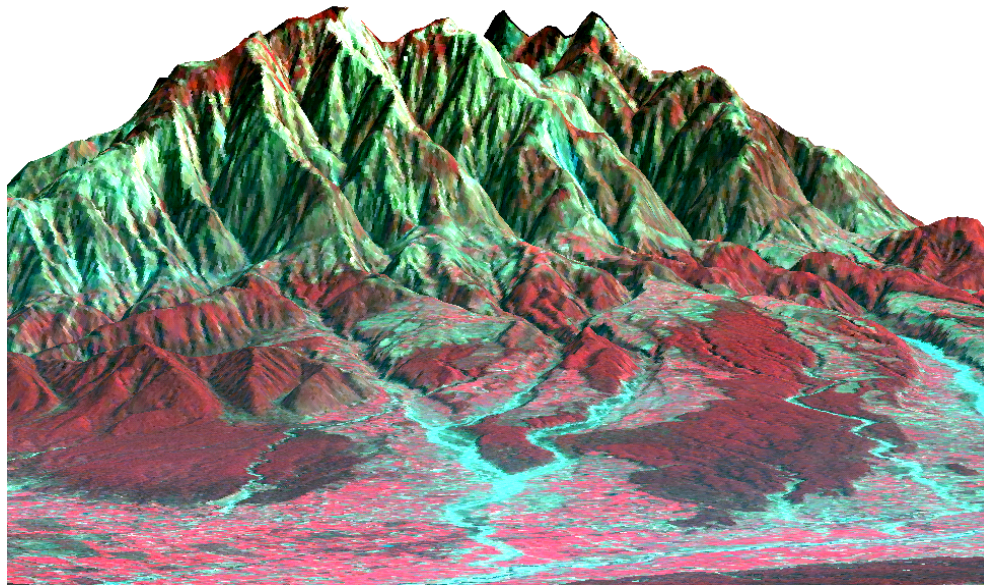
Figure 4-5 Aster Level-5 DEM draped with georeferenced Aster FCC image

4.2.2.4.　　　　DEM generation from 20 m interval contours

A 20m interval contour was used to generate a DEM using the topogrid command in arc info workstation. The output grid size specified was 12.5 meters. Output grid size was fixed at 12.5 meters to maintain the same pixel size as that of the ASAR data in the range and azimuth spacing. The generated DEM was then validated using the GCPs collected in the field. On validation, it was found that the RMSE between the observed heights and the extracted heights from the Topo-DEM was 30.24 meters.

Based on the evaluation of the RMSE of the heights from the aster level-5 DEM and the Topo-DEM with that of the observed heights, it was decided to use the aster level-5 DEM for further processing in this study.

4.2.3.　　　　ASAR alternating polarization precision image processing

The present study required that the absolute calibration of the ASAR data be done with a high level of accuracy. Some of the major issues involved in the accurate calibration of ASAR data are the georeferencing of the data sets and the calculation of the local incidence angle for the derivation of the backscattering coefficients. The following sub-sections describe in details the methods and the procedures adopted to address these issues.

4.2.3.1.　　　　Georeferencing of the ASAR datasets

The present study carried out with ASAR data required that the datasets be georeferenced with an accuracy that cannot be achieved with the help of feature matching techniques. For the purpose of georeferencing the ENVISAT ASAR data, corner reflectors were installed in the field. To corner reflect, only two surfaces meeting at a 90 degree angle must be pointed towards a beam. A triangular trihedral corner reflector presents three reflective surfaces arranged at 90-degree angles and requires less precision in pointing the reflector towards the radar beam (Fuller and Wampler, 1970). The

trihedral corner reflectors were designed such that, the opening of the reflectors forms an equilateral triangle with 8' per side. The angle from the bore sight to the reflectors plates is 30 degrees. The bottom point of the reflector is set on a circular stand that allows the reflector to be moved azimuthally as well as to be elevated to the desired elevation angle. The circular stand is fixed into the ground such that the bottom point of the corner reflector is at ground level. The exact position of the reflectors was determined using a Global Positioning System (GPS). These positions were then forwarded to the European Space Agency according to which they supplied the azimuth angle as well as the elevation angle at each position to which the corner reflectors must be oriented in order to face the ASAR beam. The distance from the ground by which the reflector had to be elevated was calculated by using the sine of the desired inclination:

$$\sin(i) = x/h \quad \textit{i.e.} \quad x = h\sin(i) \quad\quad\quad\quad\quad\quad \textbf{Equation 4-5}$$

Where i is the inclination angle (elevation angle – angle of bore sight to the reflector plate), h is the height of the reflector, and x is the perpendicular distance from the reflector base to the ground. A total of 5 such corner reflectors were installed in the field. These corner reflectors were distributed in such a way so as to cover the entire study area and to allow maximum accuracy at the time of georeferencing. The positions of the corner reflectors were selected in those areas that would have a lower decibel value as compared to the corner reflector's radar cross section thus facilitating their easy identification in the image. In addition to these, accurate points identified in ETM pan orthorectified image were also used for georeferencing. Figure 4-6 gives a snap shot of the corner reflectors installed in the field along with the corner reflectors identified in the ASAR image.
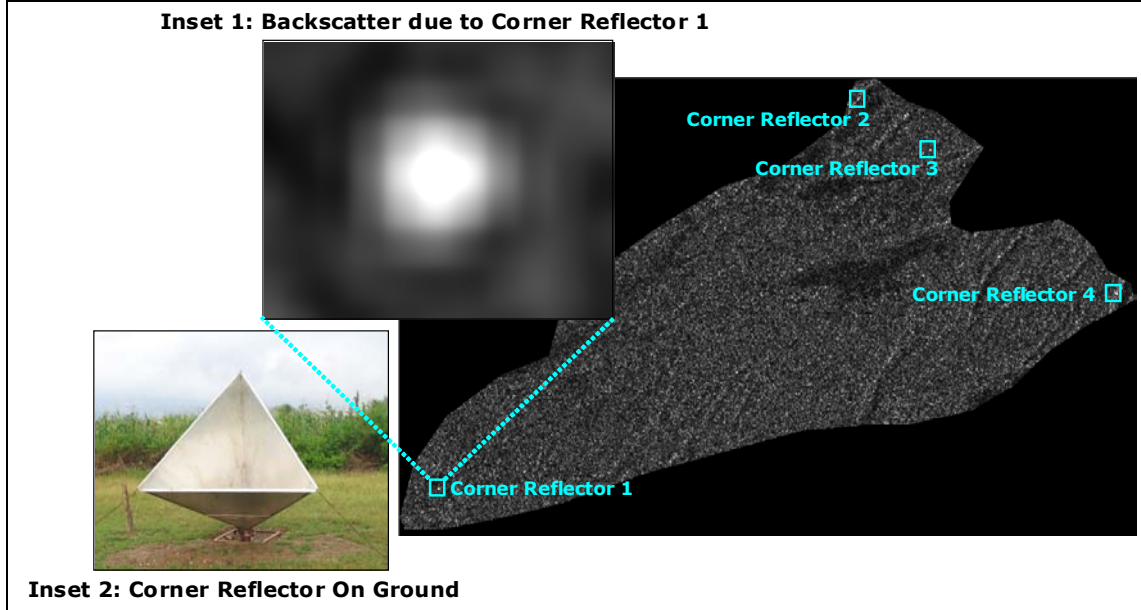
Figure 4-6 Corner Reflector Installed in field and identified in image

The georeferencing of the radar image was done using a polynomial second order equation. The RMS error achieved for the different data sets on georeferencing is given in table 4-9

Table 4-9 RMS error achieved on georeferencing the ASAR data

Sl	Polarization	Acquisition date	Swath	RMSE (X)	RMSE (Y)	Total RMSE
1	HH/HV	8/5/2006 4:57	I2	0.5740	0.1027	0.5831
2	VV/VH	8/18/2006 4:49	I4	0.3875	0.2430	0.4574
3	VV/VH	8/21/2006 4:54	I2	0.2551	0.5338	0.5916
4	HH/HV	8/26/2006 16:48	I4	0.4481	0.3659	0.5785
5	HH/HV	8/10/2006 16:51	I6	0.0926	0.3080	0.3216
6	HH/HV	8/29/2006 16:54	I6	0.4268	0.2271	0.4834
7	VV/VH	10/3/2006 16:54	I6	0.2129	0.1462	0.2583
8	VV/VH	10/19/2006 16:51	I6	0.1570	0.2083	0.2609
9	HH/HV	10/24/2006 4:43	I6	0.2932	0.3413	0.4500
10	HH/HV	10/16/2006 16:45	I4	0.4000	0.4229	0.5821
11	VV/VH	9/25/2006 4:54	I2	0.2253	0.3982	0.4575

4.2.3.2. Calibration of ASAR data

A detailed knowledge of the local incidence angle is required to perform the absolute image calibration and to derive the radar backscattering coefficients for detected ground range products. Since this information is usually not available at the processing time, a "flat terrain" is assumed during processing (based on the ellipsoid WSG84) and the final intensity image is therefore proportional to the radar brightness of the illuminated scene (Rosich and Meadows, 2004). The relationship between the value of the image pixels ("DN") and the radar backscattering coefficient (σ_0) can be written as

$$\sigma_{i,j}^0 = \frac{DN_{i,j}^2}{K} \sin(\alpha_{i,j})$$
Equation 4-6

for   i=1,2,3,……,L and j=1,2,3,……..,M
Where

K   = Absolute calibration constant

$\alpha_{i,j}$ = local incidence angle at image line and column "i, j"

$\sigma_{i,j}^0$ = Backscattering coefficient at image line and column "i, j"

$DN_{i,j}$ = Pixel intensity value at image line and column "i, j"

L, M   = Number of image lines and columns

To convert sigma nought from linear units to decibels the following equation was implemented

$$\sigma_{i,j}^0(db) = 10.\log_{10}(\sigma_{i,j}^0)$$
Equation 4-7

where

$\sigma_{i,j}^0$ = Backscattering coefficient at image line and column "i, j" and db = Decibels

4.2.3.3. Derivation of the local incidence angle

To derive the local incidence angle for each pixel in the study area equation 4-8 was used. *(SU and Troch, 1997)*

$$\alpha_{(i,j)} = \cos^{-1}\left(\cos\theta_{(i,j)} \cos\gamma_{(i,j)} + \sin\theta_{(i,j)} \sin\gamma_{(i,j)} \cos\left(\tau - \beta_{(i,j)}\right)\right) \qquad \textbf{Equation 4-8}$$

where

$\alpha_{(i,j)}$ = local incidence angle, $\theta_{(i,j)}$ and $\beta_{(i,j)}$= Slope and aspect angle respectively of the pixels derived from the aster Level-5DEM, $\gamma_{(i,j)}$ = zenith angle of sensor defined as the angle between the sensor and the normal to the horizontal surface at that location, τ = Actual flight track of the sensor. The parameters τ and β are defined to be zero to the north and increasing clockwise. The local zenith angle of the sensor is calculated using equation

$$\gamma_{(i,j)} = \cos^{-1}\left(\left(H_1 - h_{(i,j)}\right)/R_{(i,j)}\right) \qquad \textbf{Equation 4-9}$$

Where H_1 is the satellite altitude in metres above the earth surface, $h_{(i,j)}$ is the local terrain elevation in metres derived from the aster level-5 DEM, $R_{(i,j)}$ is the slant range distance to the pixel. To calculate the slant range for each pixel the two way slant range time for the 11 sample pixels in the ground range product header file were extracted and plotted against the corresponding pixel numbers. A polynomial second order equation was fitted to this plot with the correlation coefficient as 1. Table 4-10 shows an example of this calculation on a set of 11 two way slant range times extracted for the range sample pixels from the header file of the data set acquired on 26th of August 2006. Figure 4-7 shows the plot and the polynomial second order equation fit for the plot.

Table 4-10 Range Sample Pixel number and 2 way slant range time in nano seconds extracted from header file of the ASAR data set

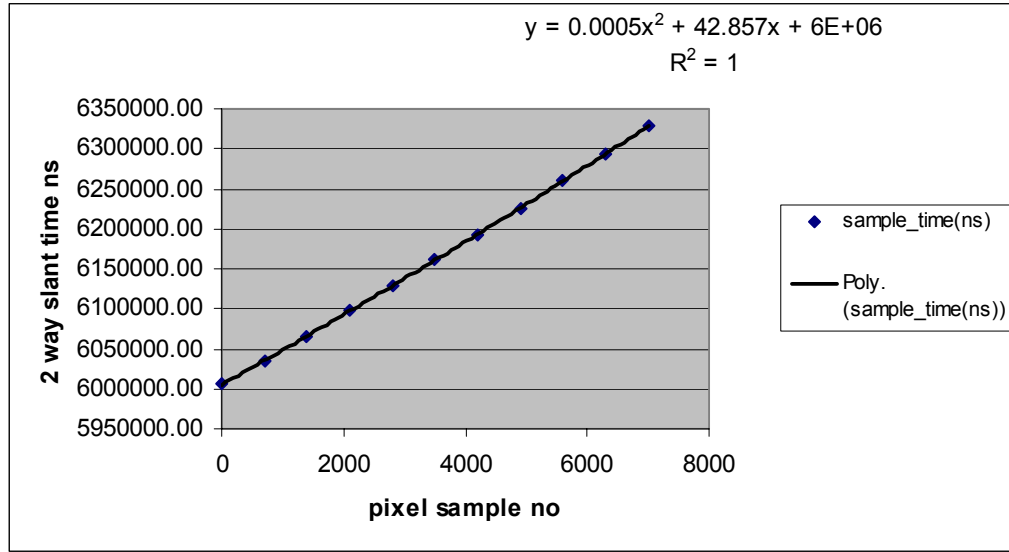| Sample No	2 way Slant range Time (ns)
1	6005299.00
701	6035473.00
1401	6066127.00
2101	6097253.00
2801	6128844.00
3500	6160847.00
4201	6193392.50
4901	6226335.50
5601	6259715.50
6301	6293524.50
6999	6327658.00

Figure 4-7 Polynomial second order equation fit to the plot of time against range sample Pixel number

To implement this second order polynomial equation, it was first necessary to extract the range pixel location (x location of the pixel in the ground range non-georeferenced image). This was done using the "PIXELX" function available in the ERDAS spatial modeler tool. PIXELX function returns a raster in which each pixel contains its column position in the ground range non-georeferenced image. The second order polynomial equation derived as shown in Figure 4-7 was then implemented using the spatial modeler tool available in Erdas® software along with a conversion factor to convert time (nano seconds) into distance thereby deriving the slant range distance to each pixel. Equation 4-11 was implemented in ERDAS spatial modeler tool for the derivation of the slant range distance to each pixel.

$$R_{(i,j)} = \left[\left(a_1 (PIXELX)^2 + a_2 (PIXELX) + a_3 \right) * 0.3 \right] \Big/ 2 \qquad \textbf{Equation 4-10}$$

Where

a_1 , a_2 , a_3 = the constants derived from the second order polynomial equation. The derived image having the slant range distance for each pixel was then georeferenced using the same second order polynomial model used to georeference the corresponding ASAR ground range precision image.

To derive the height of the sensor above the surface of the earth in equation 4-10, equation 4-12 and equation 4-13 were used. The distance from the satellite to the earth center (Rsat) was derived from the mid-azimuth satellite sate vector positions (i.e. the 3rd state vector position provided in the header file of the ASAR ground range dataset) (Rosich and Meadows, 2004)

$$Rsat = \sqrt{x^2 + y^2 + z^2} \qquad \textbf{Equation 4-11}$$

Where

x , y , z = The satellite positions on each axis

The local radius of the earth (R_e)was calculated using equation 4-13 (Ivan, 1999)

$$R_e = \left(1 - k_{flat} \sin^2(Lat)\right) R_a \qquad \textbf{Equation 4-12}$$

Where

k_{flat} = Earth flatness constant = 1/298.257

Lat = ASAR scene centre latitude

R_a = Semi-major axis of the earth = 6378.1363 km

The height of the sensor from the earth surface

$$H_1 = Rsat - R_e$$ **Equation 4-13**

This value was then used in equation 4-9 which was then implemented in Erdas model maker to derive the local zenith angle for each pixel. The average sub-satellite track heading τ was calculated from the 11 range sample pixels extracted from the header file of the corresponding ASAR ground range precision data set. The output of equation 4-9 was then used in equation 4-8 along with the derived slope and azimuth angle maps to generate the local Incidence angle images for the study area. Figure. 4-8 shows a snap shot of the local incidence angle generated for the ASAR ground range precision image acquired on 26th of August 2006.
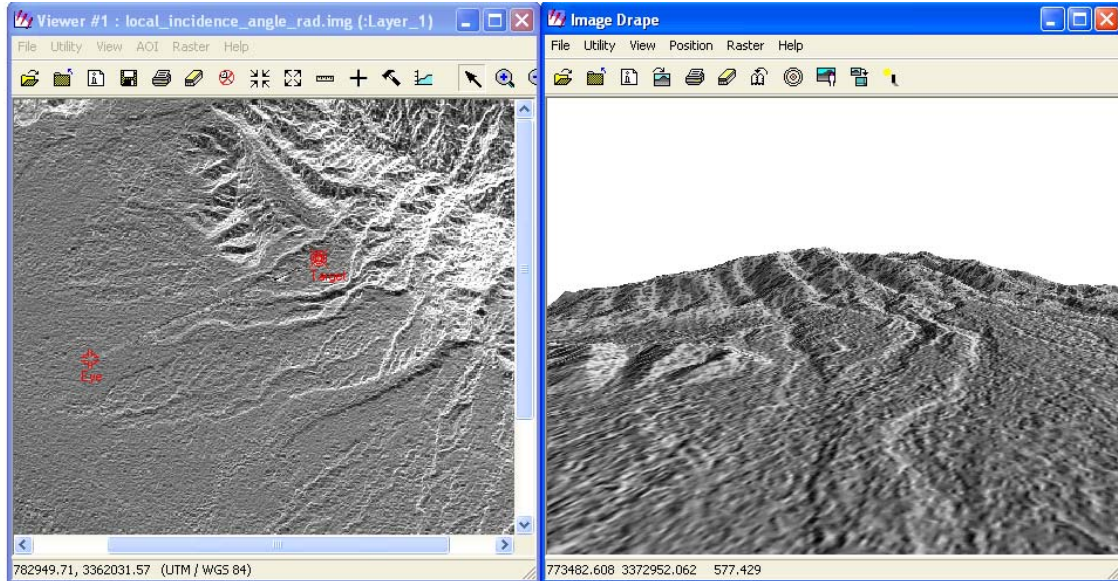
Figure 4-8 Local Incidence angle draped over Aster Level-5 DEM

The derived incidence angle images were then used as an input in equation 4-6 to derive the linear backscattering coefficient values. Which were then converted into decibel units using equation 4-7. Figure 4-9 shows a flow chart of the absolute calibration of ASAR data implemented in ERDAS modeler. Figure 4-10 shows the backscattering coefficient $\sigma^0_{hh}(db)$ and Figure 4-11 shows the backscattering coefficient $\sigma^0_{hv}(db)$ for the ASAR ground range precision image acquired on 26th of August 2006. The local incidence angle and the backscattering coefficients of all the acquired ASAR data sets were derived using the above mentioned procedure.
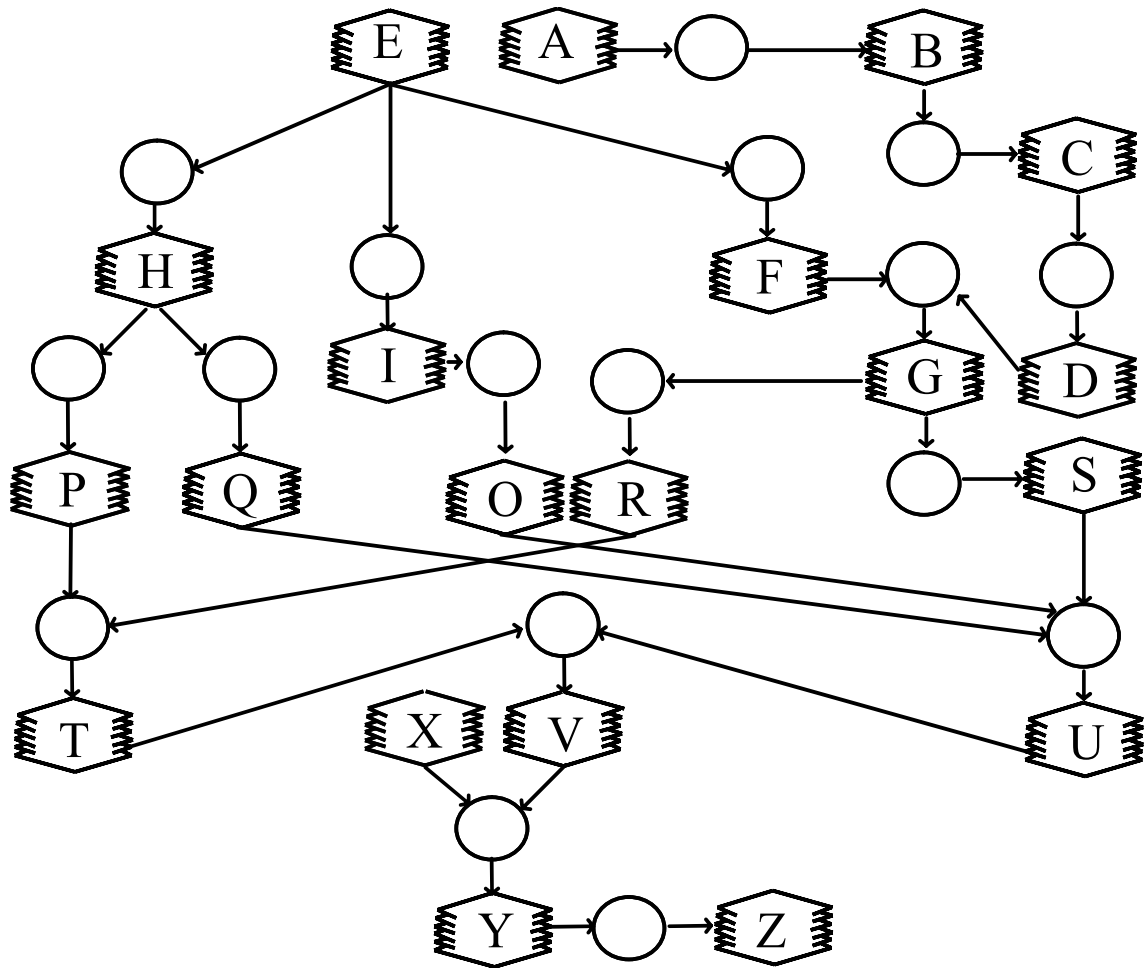
Figure 4-9 Simplified Flow Chart for absolute calibration of ASAR dataset

A- Non-georeferenced ASAR Image,

B- PIXELX (image x-co-ordinate)

C- Slant Range Distance (meters)

D- Georeferenced Slant range image

E- Level-5 Aster DEM

F- Satellite Height from terrain surface

G- Local Zenith Angle image

H- Slope Map

I- Aspect Map

O- Cosine image of (flight azimuth – I)

P- Sine Image of L

Q- Cosine image of L

R- Sine image of G

S- Cosine image of G

T = P x R

U = Q x O x S

V = Local Incidence Angle image

X = Georeferenced ASAR dataset

Y = Backscattering coefficient (linear values)

Z = Backscattering coefficient (dB values)
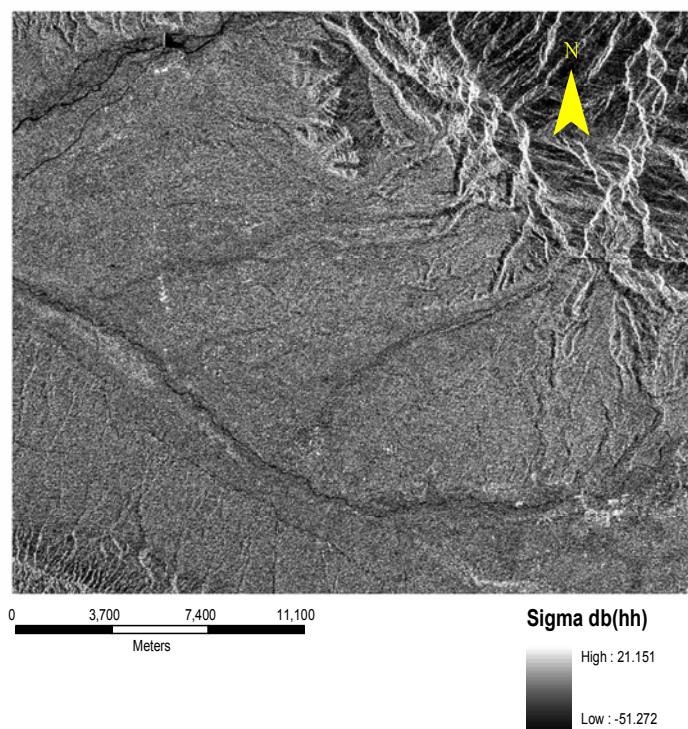
Figure 4-10 Derived Sigma dB (HH) from ASAR ground range precision image
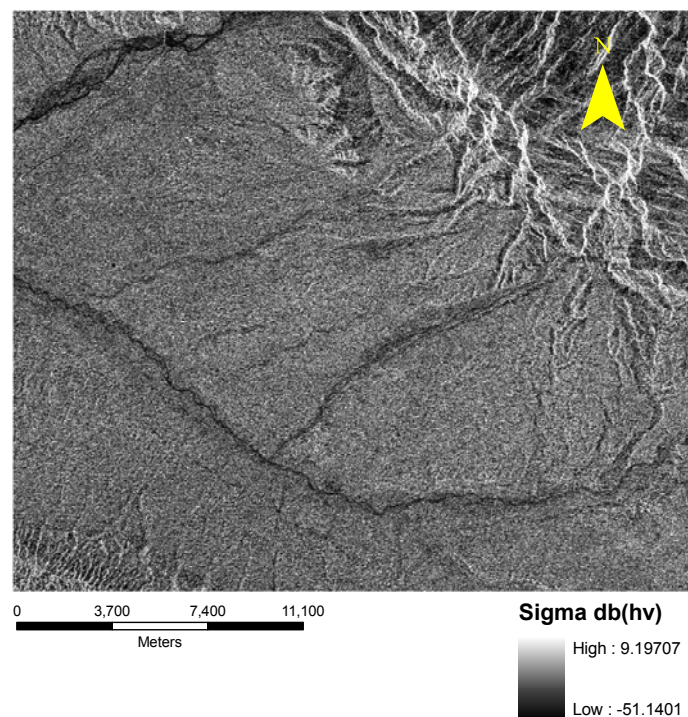
Figure 4-11 Derived Sigma dB(HV) from ASAR ground range precision image

4.2.4.   Optimization of polarization and incidence angle configurations

The Backscattering coefficients (dB values) derived for all acquired data sets were extracted for each of the sampling points. The correlation coefficients were then estimated between the extracted values *db* values for each sample point (for all incidence angles and polarizations) and the measured surface roughness, crop heights, volumetric moisture contents and soil pH. Further analyses of the correlation coefficients were carried out to decide the optimum configuration of polarization and incidence angles for estimation of surface roughness in sloping terrain. Also the influence of the various parameters on the backscattering coefficients was analysed. The results of the analysis are presented in chapter 5. Figure 4-12 gives a brief overview of the methodology followed in the present study.
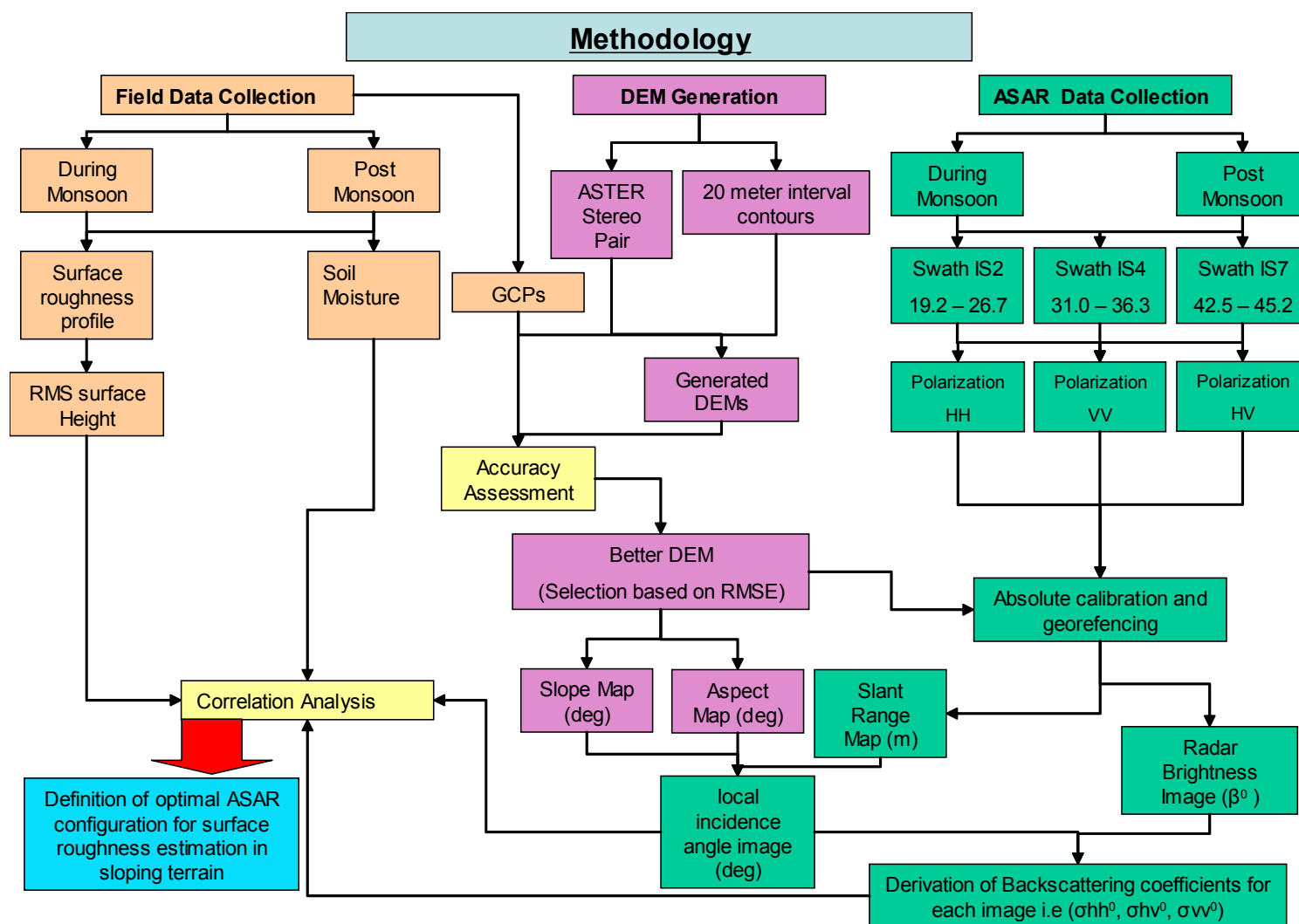
Figure 4-12 Overview of the methodology

5. Results and Discussions

The backscattering coefficients extracted for each of the sample points were analysed for their correlation with each of the field measured observations during the satellite pass. The following sections give a description of the analysis performed along with the results and their interpretation. Based on the results obtained an optimal configuration for polarization and incidence angle under consideration in this study is recommended for the estimation of roughness parameter from ENVISAT ASAR alternating polarization precision images in sloping terrain. The influence of each of the measured surface parameters on the backscattering coefficients (dB values) for different available polarizations and incidence angles is analysed separately and discussed in the following sections.

5.1.   Influence of RMS height on Backscattering coefficients (dB values)

The in field observations for the surface roughness parameter was carried out during monsoons (wet) in the month of august and also during the post monsoon (dry) season i.e. in the last week of September and during October. During monsoon the agricultural fields were cropped and therefore the crop height observations were recorded (discussed in section 4.2.1.2) as an indicator for surface roughness. The influence of the variation in crop heights on the backscattering coefficients for each of the incidence angles at all available polarizations is analysed and discussed in section 6.1.1. During the post monsoon session the surface height variations were recorded (discussed in section 4.2.1.2) in fields that were harvested along with the crop height in the remaining fields. The influence of their variations on the backscattering coefficients at all incidence angles and polarizations taken into consideration for this study are discussed in section 6.1.2. The influence of the variations in the moisture content on backscattering coefficients are also analysed and discussed in section 6.2. Finally based on the analysis an optimal configuration for incidence angle and polarization is recommended in section 6.3.

5.1.1.   Analysis of during monsoon datasets and observations

In a study of RADARSAT-1 imagery acquired over Ottawa, Ontario, results indicated that backscatter was sensitive to changes in crop variables such as biomass and growth stage. A preliminary examination of airborne CV-580 data also acquired over the site suggested that sensitivity to differences in plant height (and perhaps other crop variables) is polarization dependent. (NRCA, 2006). For the present study the influence of crop height specific to the major two crops (i.e. maize and Paddy) cultivated in the selected sample fields were analysed separately for their influence on the backscattering coefficients.
.

5.1.1.1.   Influence of RMS crop height on backscattering coefficients

The RMS heights calculated for paddy ranged from 6.64 cm to 11.01 cm. Table II-A shows the RMS height calculated for paddy along with the derived backscattering coefficients for all incidence angle ranges and polarization configurations considered in the study. The table also gives the correlation

coefficients calculated for each of the configuration against the RMS height of paddy crop. The correlation coefficients range from –0.1 to 0.5. For the during monsoon data sets it was observed that there was no relation between the crop heights in case of paddy and the derived dB values for any of the incidence angles and polarizations under consideration as can be seen in figures 5.1 to 5.5 . One possible reason for this could be the high moisture content in paddy fields during the time of the satellite passes.

Figure 5-1   Influence of RMS crop height on dB values at IS-2 (19.2 - 26.7 deg) for HH and HV polarizations

Figure 5-2   Influence of RMS crop height on dB values at IS-4 (31.0 - 36.3 deg) for HH and HV polarizations

Figure 5-3 **Influence of RMS crop height on dB values at IS-6 (39.1 - 42.8 deg) for HH and HV polarizations**

Figure 5-4 **Influence of RMS crop height on dB values at IS-2 (19.2 - 26.7 deg) for VV and VH polarizations**
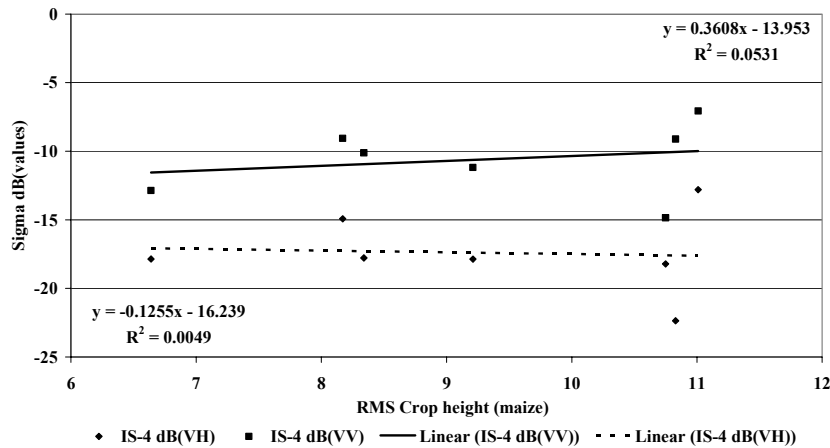
Figure 5-5   Influence of RMS crop height on dB values at IS-4 (31.0 - 36.3 deg) for VV and VH polarizations

In case of maize also it was observed that the correlation coefficients were low (R ranged from 0.1 to 0.5) between the RMS height (range from 26.07 to 71.76 cm) and dB values for all incidence angle ranges at all HH and HV polarization configurations (shown in Table II-B). Figures 5-6, 5-7 and 5-8 show the plots for the RMS crop height in case of maize for swaths IS-2, IS-4 and IS-6 at HH and HV polarizations. As seen in Figure 5-10, in case of VH polarization configuration for swath IS-4 (31.0 - 36.3 deg) it was observed that the RMS crop height for maize was weakly correlated (R = 0.6) with the db Values. Observation of the linear trend line fitted to the plot shows that the dB values increased with an increase in the RMS crop height.   Similar relation could not be seen in case of VV polarization. Also no relation between RMS height and dB values could be seen for swath IS-2 at VV or VH polarizations figure 5-9. The inability to establish a strong relation between the crop heights and dB values could be attributed to the high moisture contents in the sample fields (discussed in section 6.2.1).

Figure 5-6   Influence of RMS maize crop height on dB values at IS-2 (19.2 - 26.7 deg) for HH and HV

Figure 5-7   Influence of RMS maize crop height on dB values at IS-4 (31.0 - 36.3 deg) for HH and HV
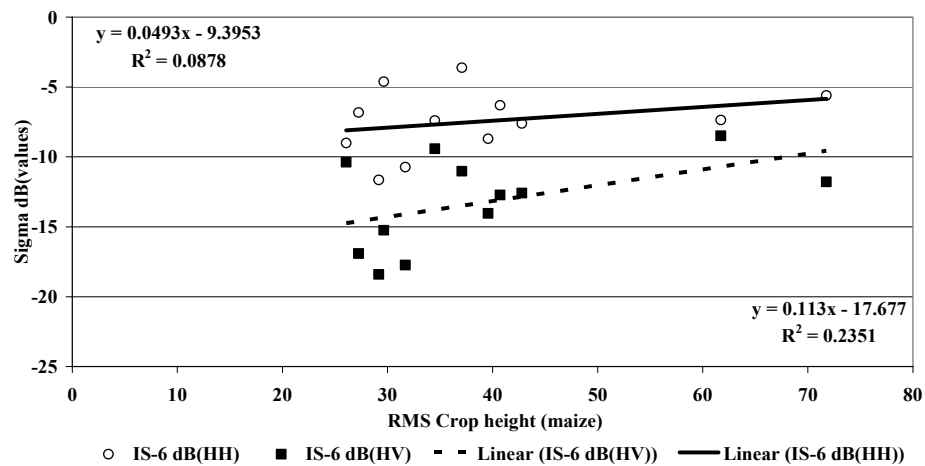
Figure 5-8   Influence of RMS maize crop height on dB values at IS-6 (39.1 - 42.8 deg) for HH and HV
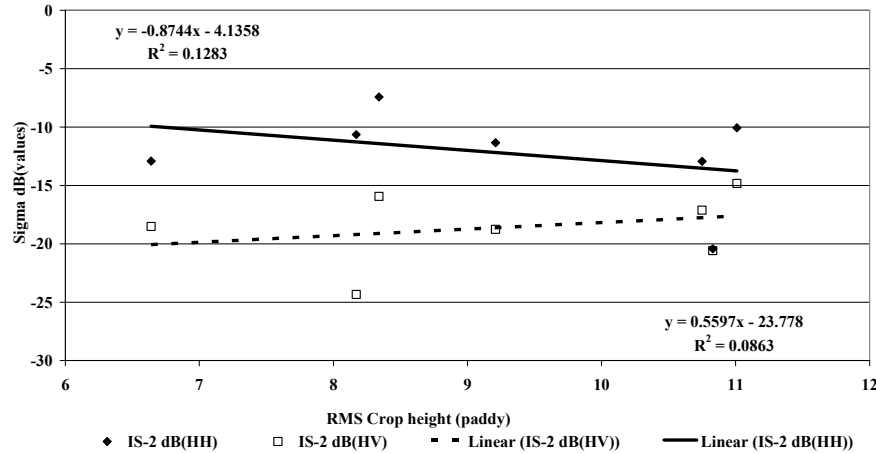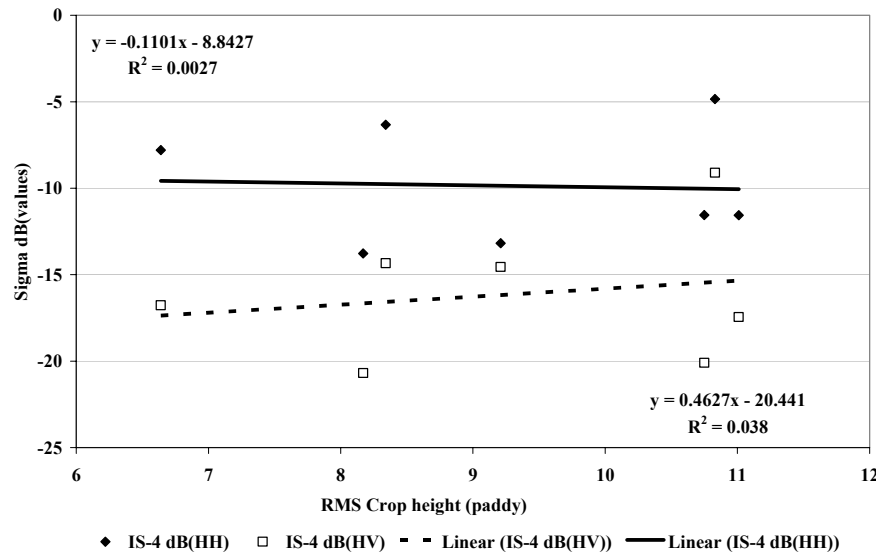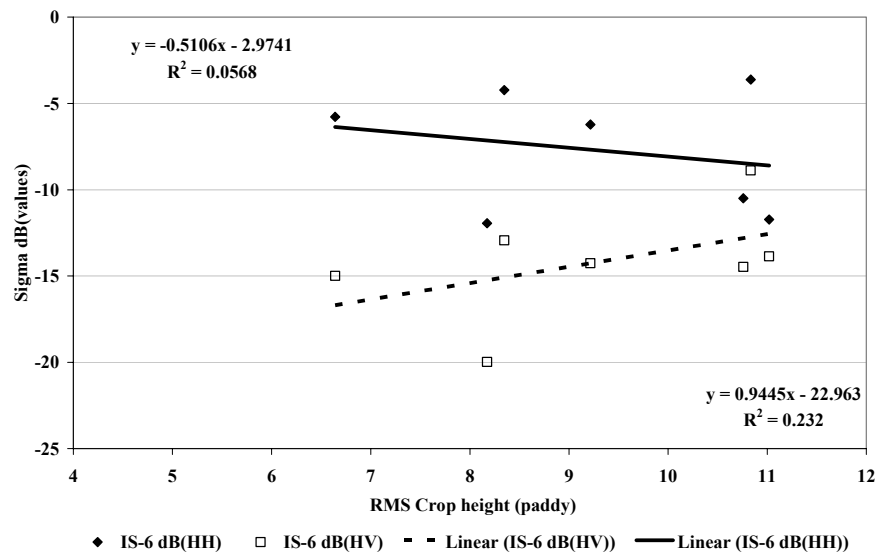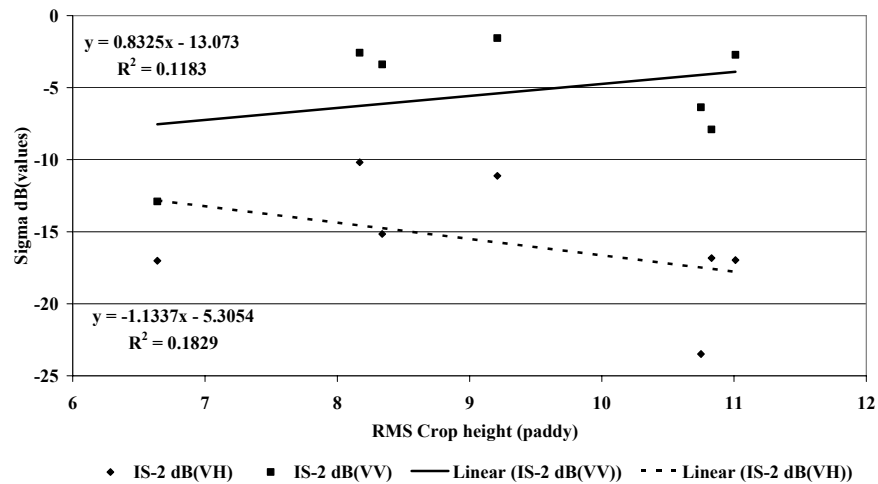

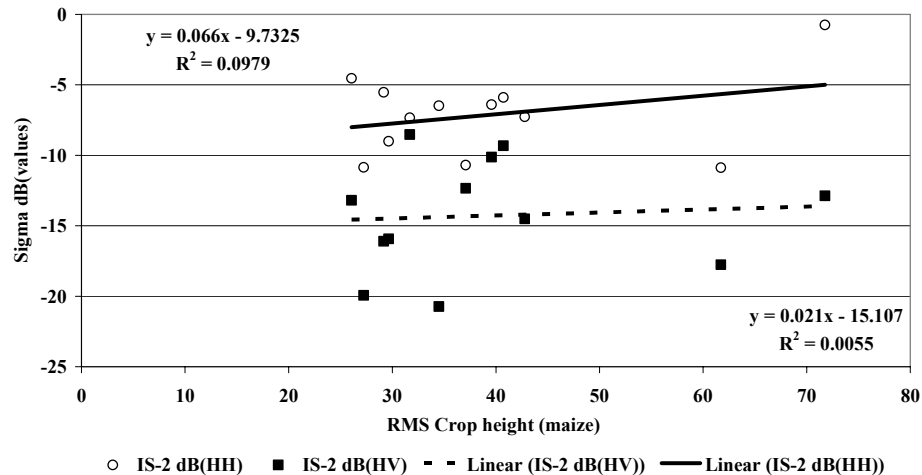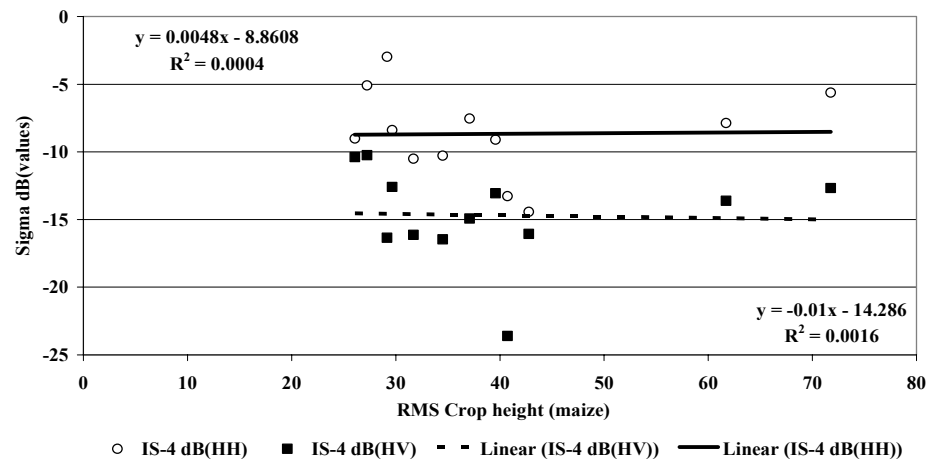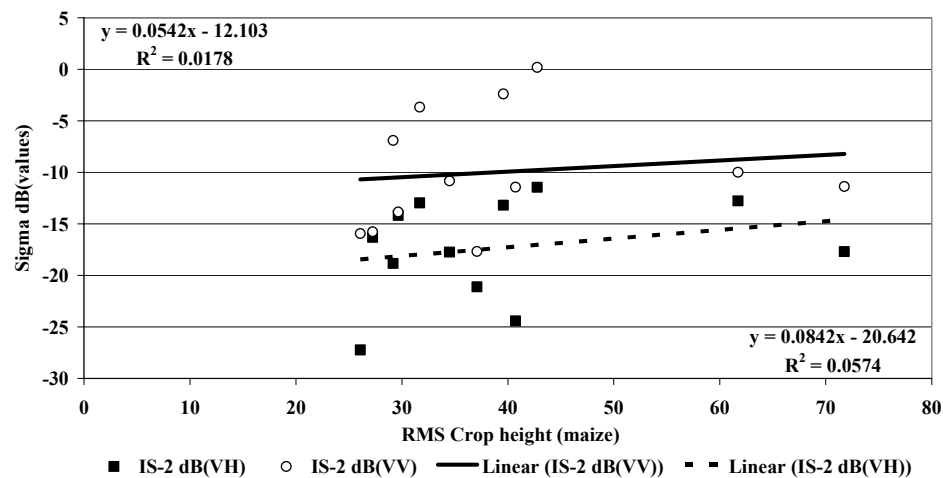**Figure 5-9   Influence of RMS maize crop height on dB values at IS-2 (19.2 - 26.7 deg) for VH and VV**
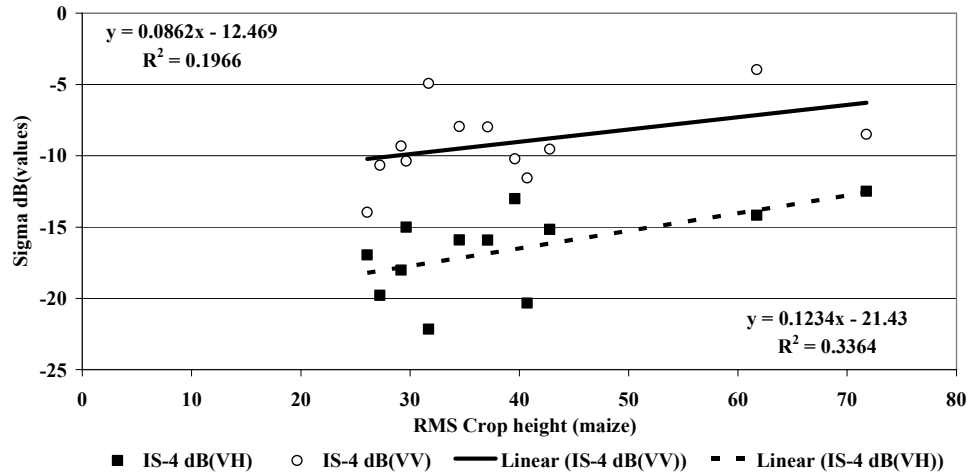
Figure 5-10 Influence of RMS maize crop height on dB values at IS-4 (31.0 - 36.3 deg) for VH and VV

5.1.2. Analysis of post-monsoon datasets and observations

During the post-monsoon session in the fields cultivated with paddy crop height measurements were taken as an indicator for surface roughness. The maize fields were harvested and initial land preparation operations were performed by farmers. Therefore surface roughness measurements for all sample fields were conducted on the first date of ASAR data acquisition and then the fields were observed for the changes in the roughness condition due to land preparation operations like ploughing and harrowing for all subsequent dates of data acquisition. Further surface roughness measurements were then conducted when a change in the roughness condition was observed. The influence of the RMS surface variations and crop height variations on the radar backscattering coefficients are separately analysed in section 5.1.2.1 and section 5.1.2.2 respectively.

5.1.2.1. Influence of RMS surface height on backscattering coefficients

From figures 5-11 and 5-12 it can be seen that for the cross polarization VH there existed a relative good correlation (R= 0.7, shown in Table II C in Appendix-II) between the measured surface variations and estimated dB values at swath range IS-2 (19.2 - 26.7^0). A linear increase in the dB values with increase in the surface roughness was seen. Similar correlation did not exist for higher swath range IS-6. A similar but inverse weak correlation (R = -0.6 shown in Table II-E in Appendix-II) was also seen between the RMS surface height and dB (values) at swath IS-4 (31.0 - 36.3^0) for cross polarization HV seen in figure 5-17. A linear decrease in dB values with increasing roughness was observed. One reason for the inverse correlation seen between VH and HV cross polarizations could be the orientation of the fields and row directions. Figures 5-13 to 5-16 and figure 5-18 shows the plots for RMS surface variations against the dB values for the incidence angles and polarization configurations under consideration in the study. Tables II-C to II-E shows the RMS surface height variations for each of the sample fields for each of the swath and polarization under consideration along with their calculated correlation coefficients.

Figure 5-11   RMSH vs Sigma dB for (VH) at IS-2

Figure 5-12   RMSH vs Sigma dB for (VH) at IS-6

Figure 5-13   RMSH vs Sigma dB for (VV) at IS-2

Figure 5-14   RMSH vs Sigma dB for (VV) at IS-6

Figure 5-15   RMSH vs Sigma dB for (HH) at IS-4

Figure 5-16   RMSH vs Sigma dB for (HH) at IS-6
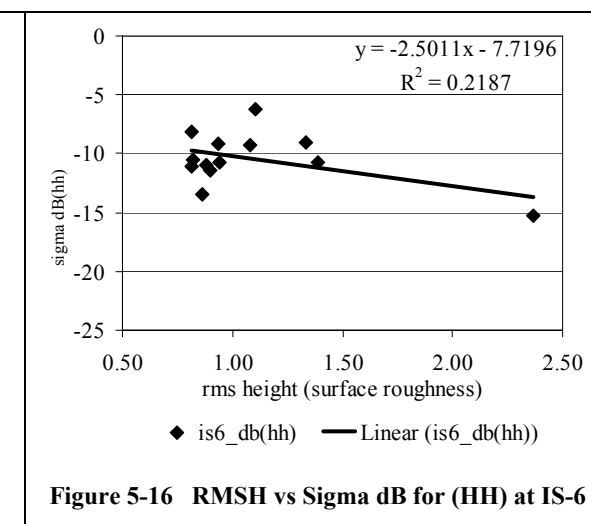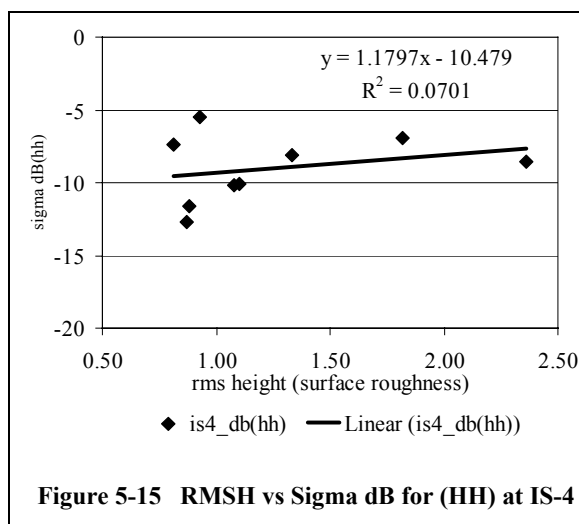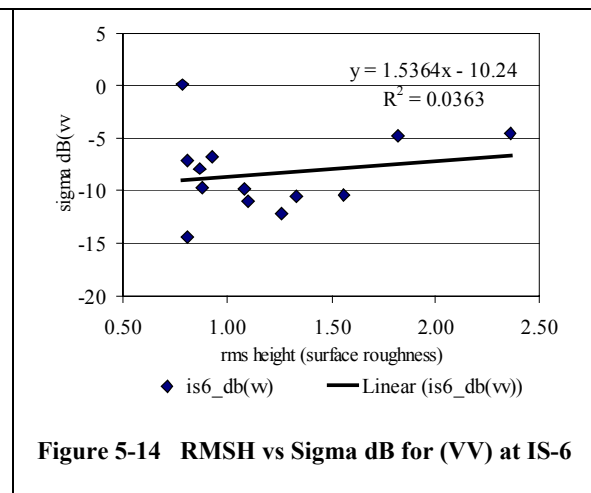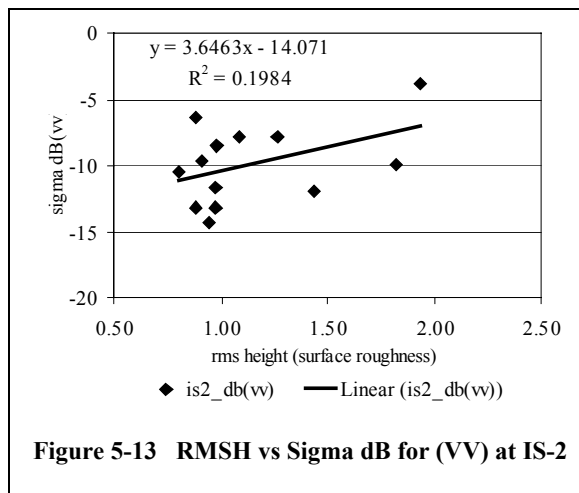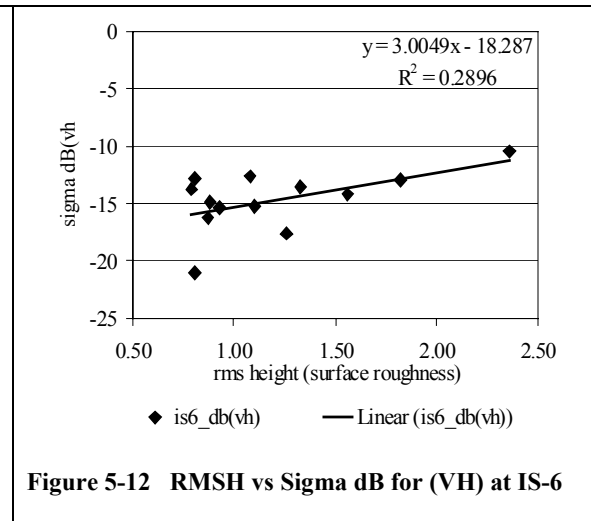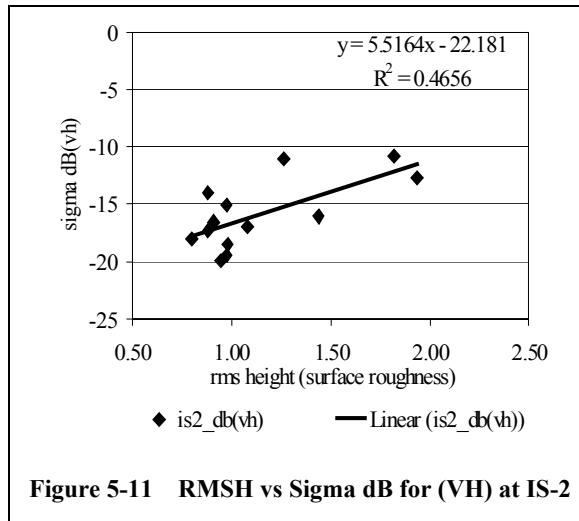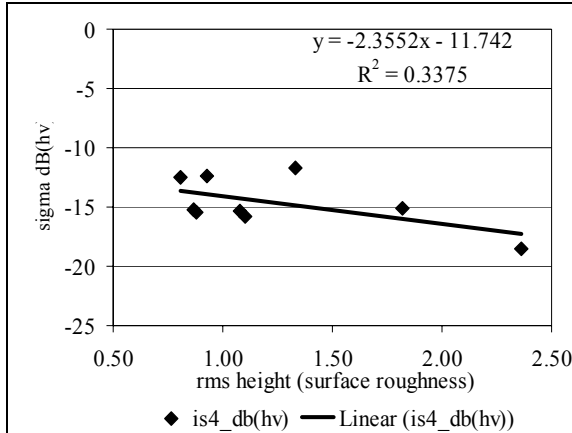
Figure 5-17   RMSH vs Sigma dB for (HV) at IS-4
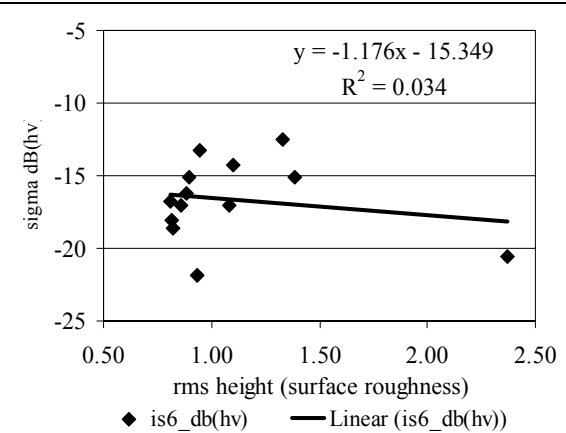
Figure 5-18   RMSH vs Sigma dB for (HV) at IS-6

5.1.2.2.   Influence of RMS crop height on backscattering coefficients

For the measured crop height observations correlation between the RMS crop heights and derived dB values were found in like polarization VV (R= 0.7, shown in Table II-G in Appendix-II) for swath IS-2 (19.2 - 26.7^0) and HH (R= 0.8, shown in Table II-G in Appendix-II) for swath IS-4 (31.0 - 36.3^0). As seen in figure 5-19 and figure 5-21 an increase in RMS crop height of paddy resulted in a linear increase in dB values for VV polarization at IS-2 and HH polarization at IS-4 respectively. Probable reason being that taller vertical crop stand resulted in increased strength of backscatter returns. For all other combinations of incidence angle and polarization configurations considered in this study, no relationship could be established between the observed RMS crop heights and derived db values. Figures 5-20 and 5-22 to 5-26 show the plots for the field measured RMS crop heights against the derived dB values for all other combinations of incidence angles and polarization configuration.

Figure 5-19 RMSH vs Sigma dB for (VV) at IS-2

Figure 5-20 RMSH vs Sigma dB for (VV) at IS-6

Figure 5-21 RMSH vs Sigma dB for (HH) at IS-4

Figure 5-22 RMSH vs Sigma dB for (HH) at IS-6
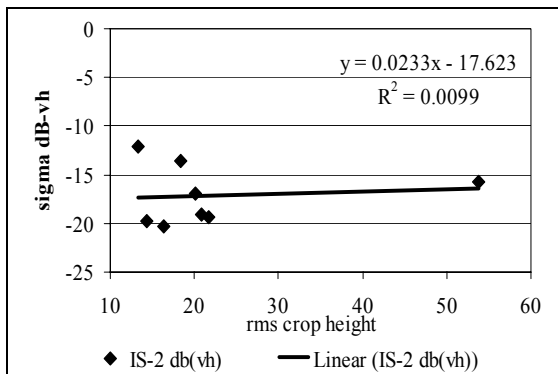
Figure 5-23 RMSH vs Sigma dB for (VH) at IS-2
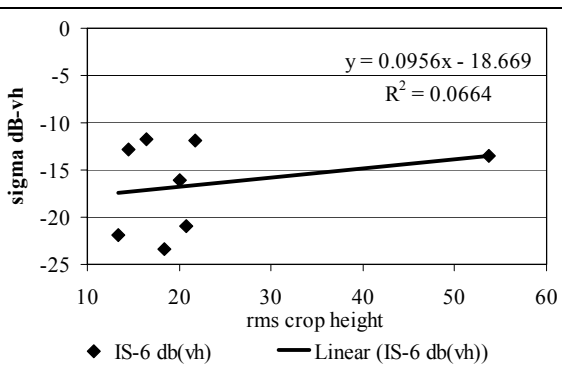
Figure 5-24 RMSH vs Sigma dB for (VH) at IS-6
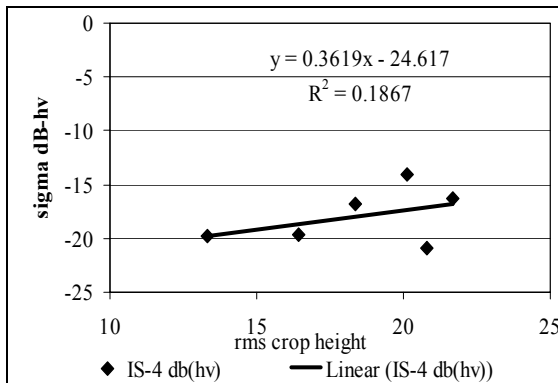
Figure 5-25 RMSH vs Sigma dB for (HV) at IS-4
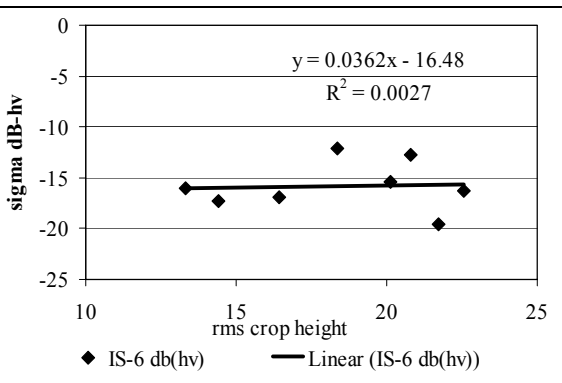
Figure 5-26 RMSH vs Sigma dB for (HV) at IS-6

5.2. Influence of Volumeteric moisture contents on backscattering coefficients (dBvalues)

The measured volumetric moisture contents in the maize fields were analysed for their influence on backscattering coefficients (dB values) for all incidence angles and polarization configurations under consideration. Section 5.2.1 contains the results and discussions for this analysis. The paddy fields being submerged were not considered in the analysis of the during monsoon datasets. During the post-monsoon session most of the paddy fields were submerged therefore only the harvested maize fields

were considered for the analysis of the post-monsoon datasets. The measurements for moisture content were done at depths of 5cm and 10 cm. The influence of the moisture contents on dB values at each of the depths is analysed and discussed in section 5.2.1

5.2.1.   Analysis of during monsoon datasets and observations

Relatively strong correlation (R= 0.8) was observed between dB values and measured volumetric moisture contents (VMC) at both depths i.e. 5cm and 10cm for HV polarization at swath IS-2 (figure 5-28). At swath IS-4 for HV polarization a weak negative correlation (R= -0.6) was observed for volumetric moisture contents at10 cm depth (figure 5-30). For Both swaths a linear relationship was observed between the measured soil moisture and the derived dB values. Tables II-H to II-L shows the VMC at 5 cm and 10 cm depths measured for each of the datasets acquired along with the corresponding derived dB (values) at all polarizations under consideration. Figures 5-27 to 5-36 show the plots for the VMC at 5 cm and 10 cm for each of the corresponding dB values for each of the swath and polarizations configuration. For all other configurations of swath and polarization no correlation between the dB values and measured VMC could be found.

Figure 5-27 VMC vs Sigma dB for (HH) at IS-2

Figure 5-28 VMC vs Sigma dB for (HV) at IS-2

Figure 5-29 VMC vs Sigma dB for (HH) at IS-4

Figure 5-30 VMC vs Sigma dB for (HV) at IS-4
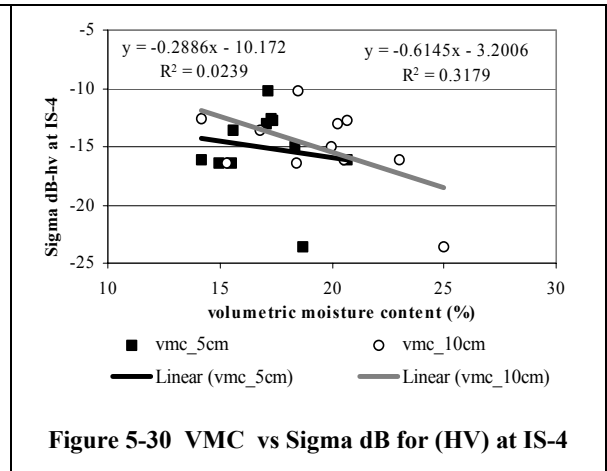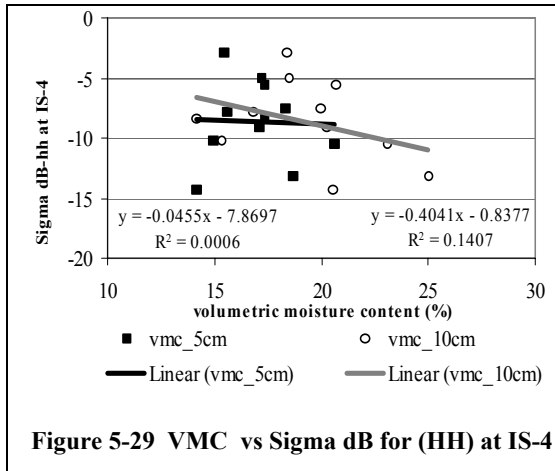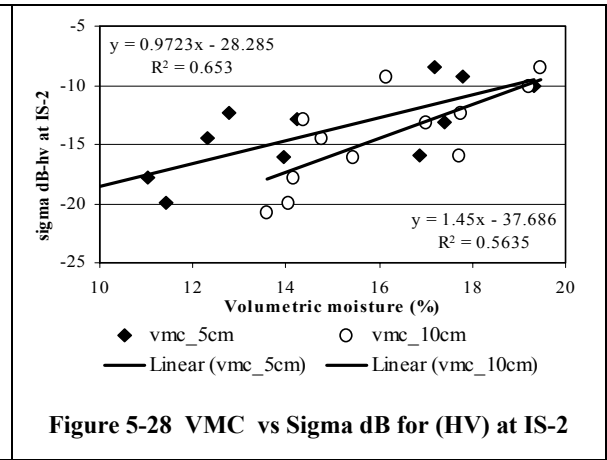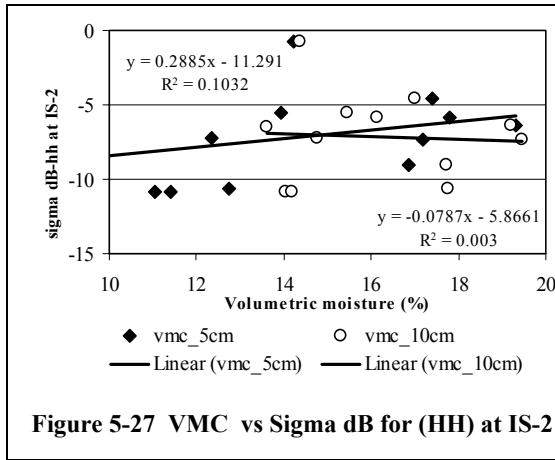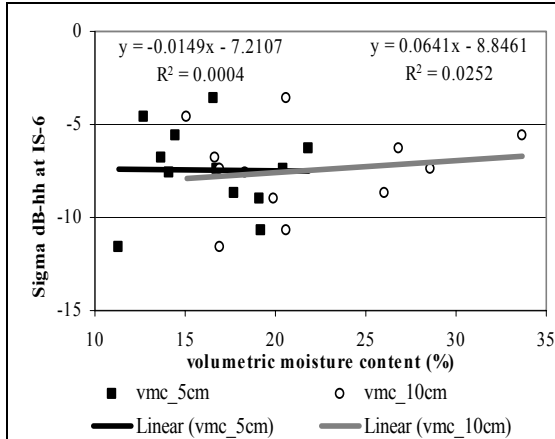
Figure 5-31 VMC vs Sigma dB for (HH) at IS-6
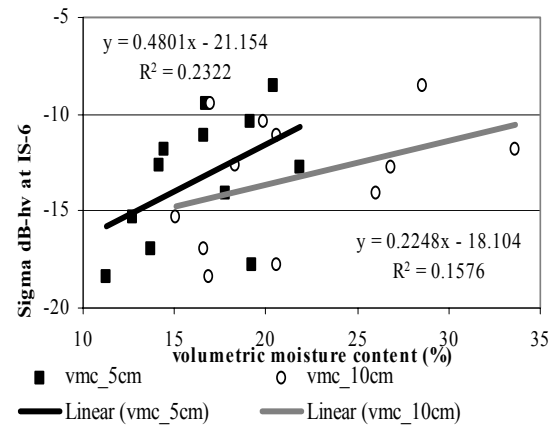
Figure 5-32 VMC vs Sigma dB for (HV) at IS-6
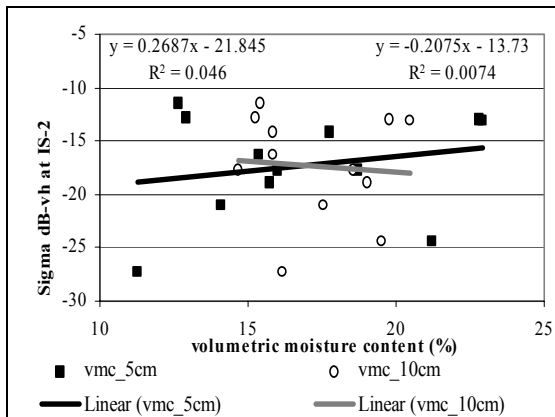
Figure 5-33   VMC vs Sigma dB for (VH) at IS-2
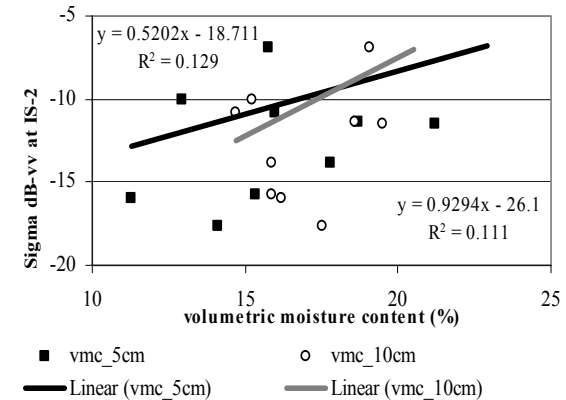
Figure 5-34 VMC vs Sigma dB for (VV) at IS-2
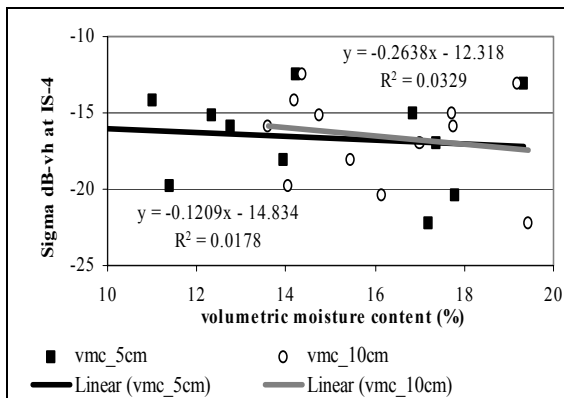
Figure 5-35 VMC vs Sigma dB for (VH) at IS-4
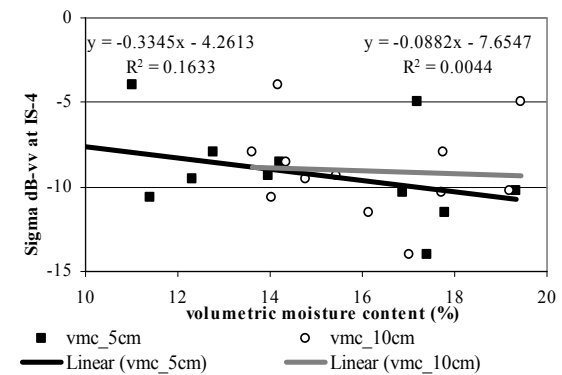
Figure 5-36 VMC vs Sigma dB for (VV) at IS-4

5.2.2. Analysis of post monsoon datasets and observations

For the post monsoon datasets it was observed that only HH polarization at IS-4 and HV polarization at IS-6 showed a relatively strong correlation with the field measured volumetric moisture contents. At IS-4 for dB values of HH polarization a correlation coefficient of R= -0.8 was observed with the VMC at 5cm depth. At IS-6 for dB values of HV polarization a correlation coefficient of R=0.6 was observed for VMC at 10 cm depth. As seen in figure 5-42 and figure 5-43 for both cases a linear relationship was seen between the db values and the VMC.

Figure 5-37 VMC vs Sigma dB for (VH) at IS-2

Figure 5-38 VMC vs Sigma dB for (VV) at IS-2

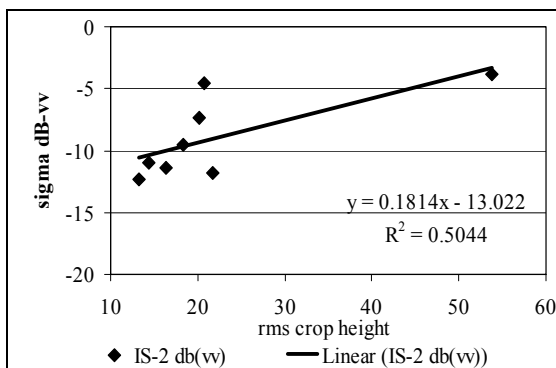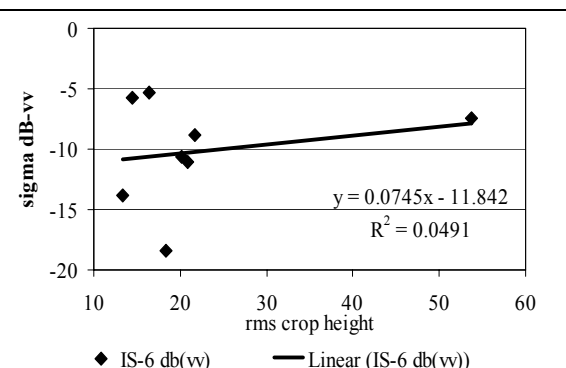
Figure 5-39 VMC vs Sigma dB for (VH) at IS-6

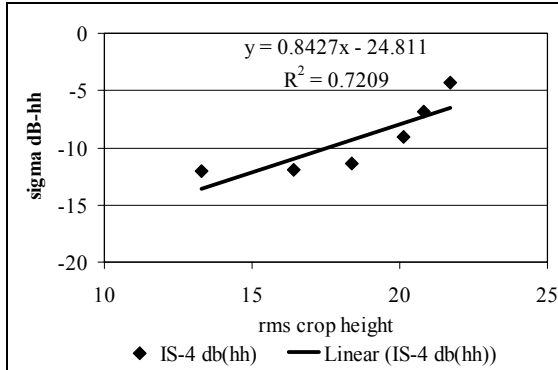Figure 5-40 VMC vs Sigma dB for (VV) at IS-6
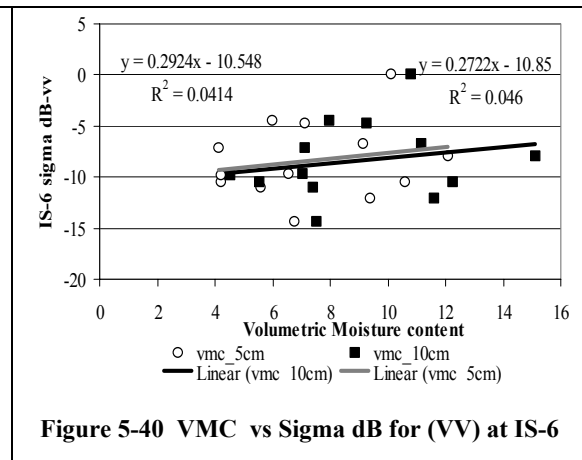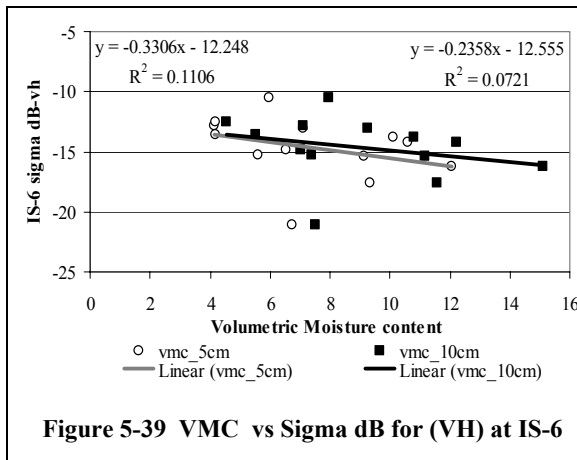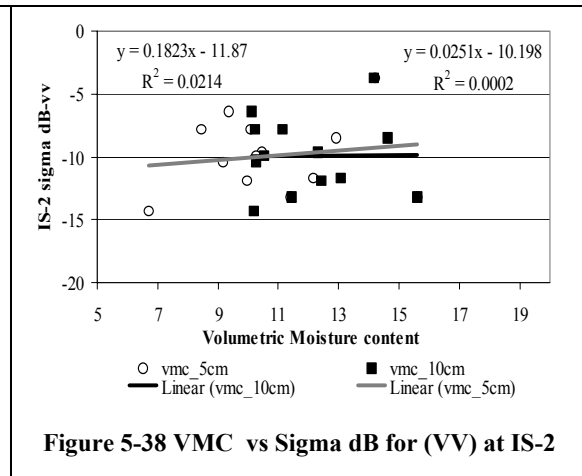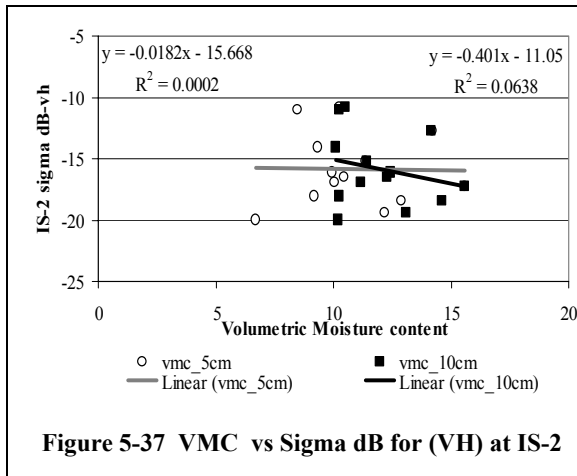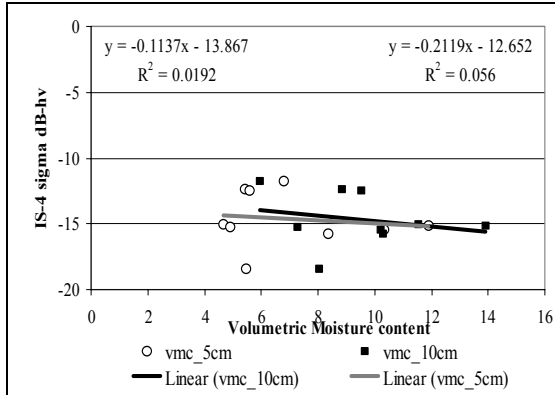
Figure 5-41 VMC vs Sigma dB for (HV) at IS-4
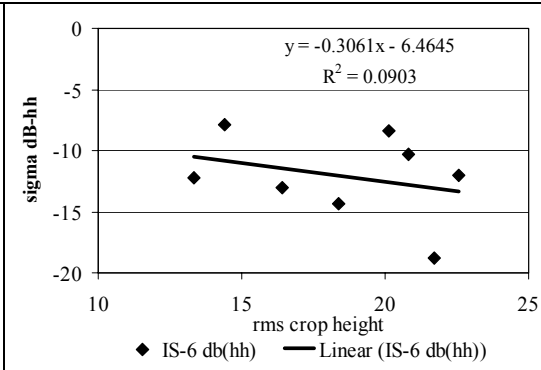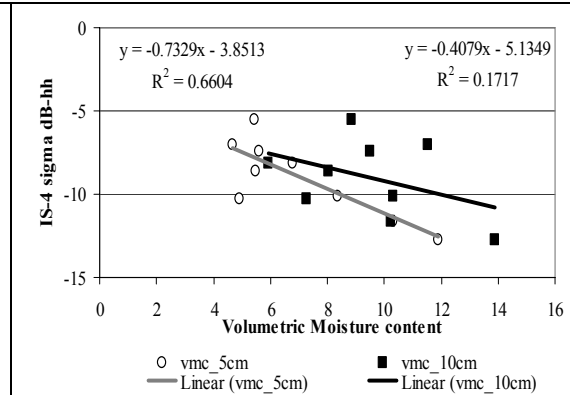

Figure 5-42 VMC vs Sigma dB for (HH) at IS-4
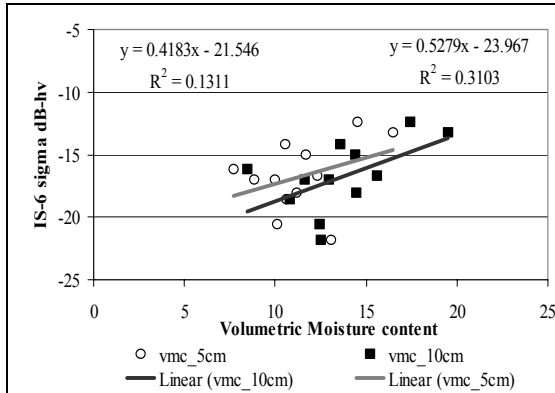
Figure 5-43 VMC vs Sigma dB for (HV) at IS-6
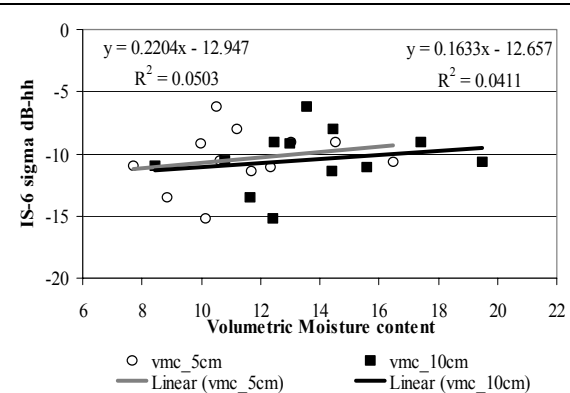
Figure 5-44 VMC vs Sigma dB for (HH) at IS-6

5.3. Selection of optimal configuration for incidence angle and polarization

From the analysis of the results given above an optimal configuration of incidence angle and polarization from those considered for the study was derived. To facilitate easy comparison a graph was plotted (figure 5-45 and figure 5-46) for the correlation values calculated for each of the surface parameters against their corresponding incidence angle and polarization configuration for during monsoon datasets as well as the post-monsoon datasets.
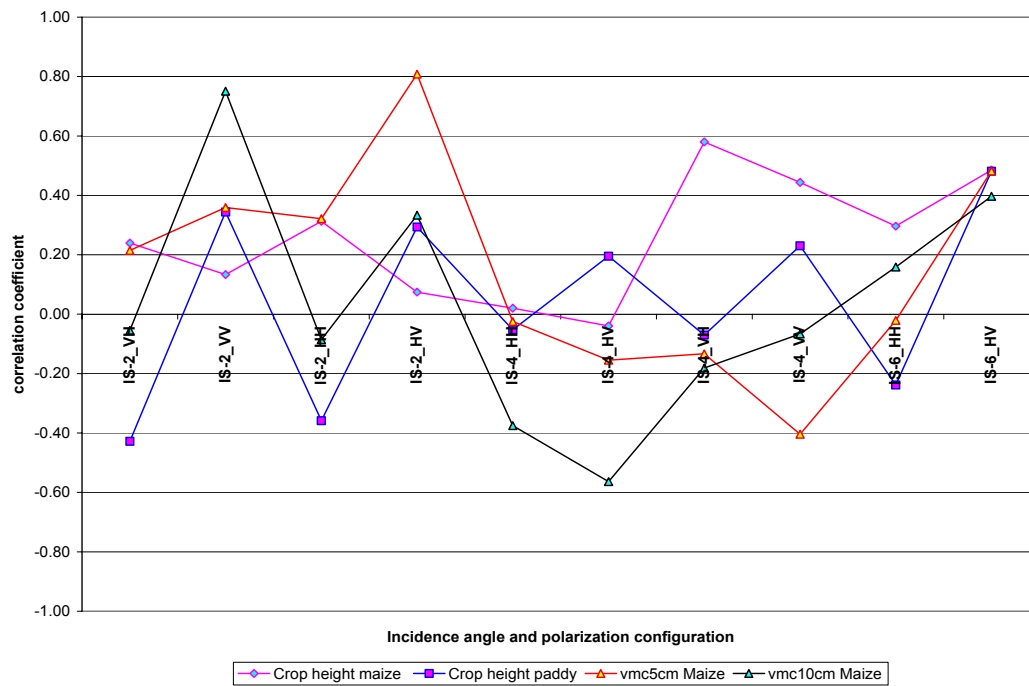
Figure 5-45   Correlation coefficients plotted for each of the surface description parameters for all configurations in during-monsoon datasets

An analysis of figure 5-45 shows that considering crop height as an indicator for surface roughness no conclusive optimization of polarization and incidence angles could be done for surface roughness. One of the reasons could be the high variability in moisture contents. Although for VH polarization at swath IS-4 a weak correlation was observed between crop height in paddy and derived dB values. At this configuration it was also observed that no correlation existed between dB and all other surface parameters. A more conclusive result was obtained in the post-monsoon datasets. From figure 5-46 it can be seen that for surface roughness estimations in sloping areas, cross polarizations VH at swath IS-2 would be best able to discriminate the soil surface vertical height variations. Considering crop height as an indicator for surface roughness it can be seen that although like polarization HH at swath IS-4 gives the highest positive correlation, there is also a corresponding high negative correlation between VMC at 5cm and dB values at the same configuration. Therefore estimations of roughness considering crop height could best be done with like polarization VV at swath IS-2, as seen in figure 5-46. Ratio of HH and VV polarizations obtained at swath IS-4 and IS-2 respectively could result in better estimation for moisture as the influence of surface roughness would be removed from the ratio.
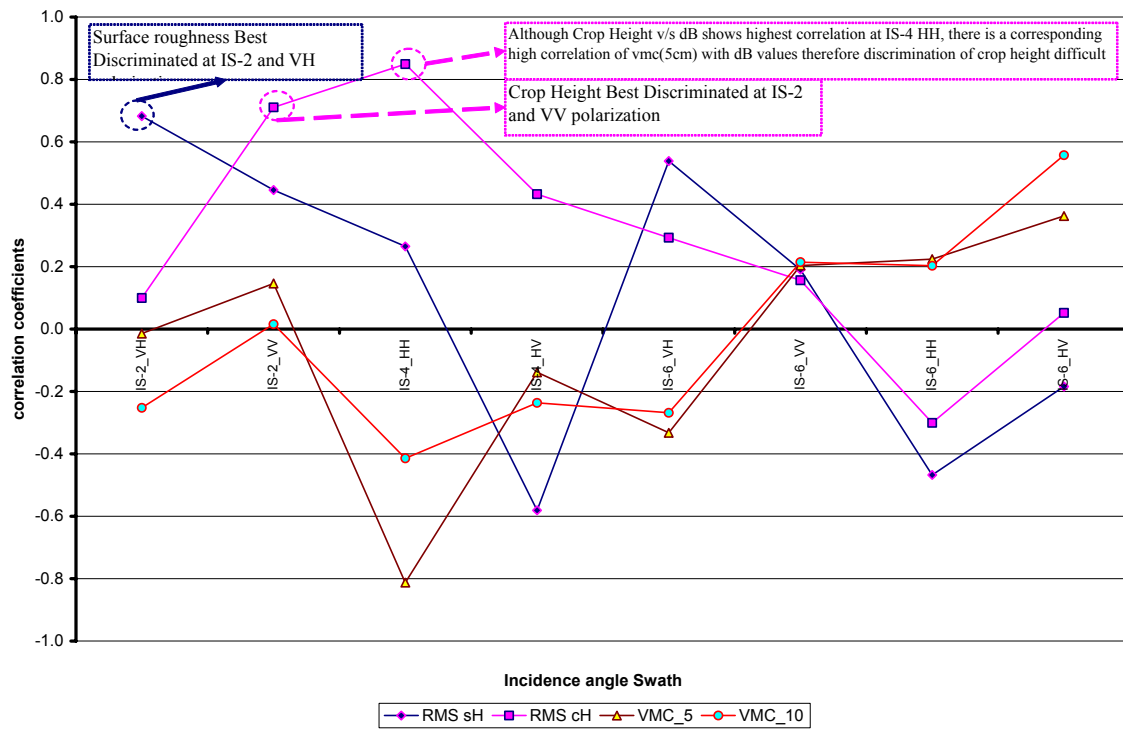
Figure 5-46 Correlation coefficients plotted for each of the surface description parameters for all configurations in post-monsoon datasets

6. Conclusions and Recommendations

6.1. Research questions addressed concerning the Objective of the study

The main Objective of the study is to establish the optimal configuration of local incidence angle and polarization for surface roughness estimation in ENVISAT-1 ASAR data. The following were the research questions addressed to meet the objective of the study.

6.1.1. Is there a correlation between lower incidence angle and backscattering coefficient of ASAR data in sloping terrain?

The prime objective of this question is to identify the range of incidence angle at which the influence of soil surface roughness would predominate over the influence of soil moisture on the ENVISAT ASAR backscattering coefficients. For the present study three incidence angle ranges were taken into consideration. i.e. IS-2 (incidence angle range from 19.2 - 26.7^0), IS-4(incidence angle range from 31.0 - 36.3^0) and IS-6(incidence angle range from 39.1 - 42.8^0). To remove the influence of local slope on the backscattering coefficients the calculation of the local incidence angle was done for each of the acquired images and subsequently the backscattering coefficients were then derived using the estimated local incidence angles. Analysis of the derived backscattering coefficients for each of the swaths and the corresponding roughness and moisture measurements showed that for sloping terrain ASAR images acquired at swath IS-2 (19.2 - 26.7^0) would be the best swath range from the three taken into consideration for the estimation of surface roughness parameters in slopping terrain.

6.1.2. Is there a correlation between VV polarization and backscattering coefficient of ASAR data in sloping terrain?

The prime objective of this question is to identify the polarization configuration at which the influence of the soil surface roughness would predominate over the influence of soil moisture on the ENVISAT ASAR backscattering coefficients. For the present study four polarization configurations HH, HV, VV, and VH were taken into consideration. The analysis of the backscattering coefficients derived for these polarization configurations and the measured soil surface roughness as well as the measured field moisture contents showed that VV and VH polarizations were sensitive to the variations in the surface roughness conditions and were dependent on the swath at which they were acquired. For crop height taken as an indicator for surface roughness it was found that HH polarizations were sensitive to the variation in crop height. But HH polarizations were also found to be sensitive to the moisture variations in the field. For slopping terrain using ASAR data VV and VH polarization in combination with optimum swath would be the best polarization configuration from the four taken into consideration for the estimation of surface roughness parameters.

6.1.3. What is the optimal combination of local incidence angle and polarization for surface roughness estimation in ENVISAT-1 ASAR data?

Based on the conclusion of the above two research questions a combined analysis of the three swaths and four polarizations was carried out to derive an optimum configuration of incidence angle and polarization for the estimation of surface roughness parameter from ENVISAT ASAR datasets in sloping terrain. Analysis of the derived backscattering coefficients for all incidence angles and polarization configurations with the measured surface parameters show that in slopping terrain ASAR data acquired at Swath IS-2 (19.2 - 26.7^0) and at polarizations of VH and VV would be the optimum configuration from those considered for the present study to estimate surface roughness. A ratio image of VV to VH acquired at swath of IS-4 and IS-2 respectively would be optimum for moisture estimations. The results of the study contribute to developing a theoretical basis for the use of inversion models for a better estimation of roughness parameters using either theoretical or physical based inversion models of estimation

6.1.4. Recommendations

- Further study using data sets acquired in a pre-monsoon sessions also would enable to develop an understanding of the influence of the seasonal variations of surface parameters on the backscattering coefficients.

- Advanced studies to estimate roughness parameter using the IEM inversion model (Hoeben et al., 1997) can give good results for estimation of surface roughness for the selected optimum configurations.

- A similar study incorporating a higher resolution DEM for the derivation of the local incidence angle can be done to find the influence of incorporating a higher resolution DEM on the derivation of Backscattering coefficients and further on roughness estimations.

7. References

Baghdadi, N., Holah, N. and Zribi, M., 2006. Soil moisture estimation using multi-incidence and
multi-polarization ASAR data. International Journal of Remote Sensing, 27(9-10): 1907-1920.

Baghdadi, N., King, C., Bourguignon, A. and Remond, A., 2002. Potential of ERS and Radarsat data
for surface roughness monitoring over bare agricultural fields: application to catchments in
Northern France. International Journal of Remote Sensing, 23(17): 3427-3442.

Beaudoin, A., Letoan, T. and Gwyn, Q.H.J., 1990. Sar Observations and Modeling of the C-Band
Backscatter Variability Due to Multiscale Geometry and Soil-Moisture. Ieee Transactions on
Geoscience and Remote Sensing, 28(5): 886-895.

Blumberg, D.G. and Freilikher, V., 2001. Soil water-content and surface roughness retrieval using
ERS-2 SAR data in the Negev Desert, Israel. Journal of Arid Environments, 49(3): 449-464.

Campbell, B.A. and Shepard, M.K., 1996. Orbital SAR and ground-penetrating radar for mars:
complementary tools in the search for water. Journal of Geophysical Research, 101(18): 941-
952.

Eckert, S. and Kellenberger, T., 2002. Qualitaetsanalyse automatisch generierter digitaler
Gelaendemodelle mit Hilfe von ASTER Daten. Publikationen der Deutschen Gesellschaft für
Photogrammetrie und Fernerkundung, Band 11, Eckhardt Seyfert (Hrsg.), 337-344 pp.

Elachi, C., 1988. Spaceborne radar remote sensing: applications and techniques. IEEE Press, New
York, 255 pp.

ESA, 2006. ENVISAT ASAR Handbook 2.1.

Fuller, J.E. and Wampler, E.S., 1970. The Lunar Laser Reflector. Scientific American, 222(3): 42.

Fung, A.K. and Chen, K.S., 1992. Dependence of the Surface Backscattering Coefficients on
Roughness, Frequency and Polarization States. International Journal of Remote Sensing,
13(9): 1663-1680.

Gómeza, J.A. and Nearingb, M.A., 2005. Runoff and sediment losses from rough and smooth soil
surfaces in a laboratory experiment. CATENA, 59(3): 253-266.

Gupta, S.C. and Kapoor, V.K., 2003. Fundamentals of Mathematical Statistics, Fundamentals of
Mathematical Statistics. Fundamentals of Mathematical Statistics, Fundamentals of
Mathematical Statistics. Sultan Chand & Sons, Delhi, 2.1-2.74 pp.

Handbook, ASTER User Handbook, Version 2.

Hirano, A., Welch, R. and Lang, H., 2003. Mapping from ASTER stereo image data: DEM validation
and accuracy assessment. ISPRS Journal of Photogrammetry and Remote Sensing, 57(5-6):
356-370.

Hoeben, R., Troch, P.A., Zhongbo Su Mancini, M. and Chen, K.-S., 1997. Sensitivity of radar
backscattering to soil surface parameters: acomparison between theoretical analysis and
experimental evidence. IEEE Transactions on Geoscience and Remote Sensing, 3: 1368-1370

Holah, N., Baghdadi, N., Zribi, M., Bruand, A. and King, C., 2005. Potential of ASAR/ENVISAT for
the characterization of soil surface parameters over bare agricultural fields. Remote Sensing of
Environment, 96(1): 78-86.

Ivan, S.A., 1999. Projecting an Arbitrary Latitude and Longitude onto a Tangent Plane. MERS 99-04,
Brigham Young University.

Jensen, J.R., 2000. Remote Sensing of the Environment: An Earth Resource Perspective. Prentice
Hall, Saddle River, 544 pp.

Kingsley, S. and Quegan, S., 1992. Understanding Radar Systems. McGraw-Hill Book Company,
London, 375 pp.

LeicaGeosystems, General Guide to Static and Rapid-Static ver 3.0.

Lewis, A.J. and Henderson, F.M., 1998. Radar fundamentals: the geoscience perspective. In: A. Lewis and F. Henderson (Editors), Principles and Applications of Imaging Radar. John Wiley New York, pp. 131-181.

Lillesand, T.M. and Kiefer, R.W., 2000. Remote Sensing and Image Interpretation. John Wiley, New York, 750 pp.

Martin, H., Wolfgang, H., ohannes, R., Small, D. and Detlev, K., 2005. TECHNICAL ASPECTS OF ENVISAT ASAR GEOCODING CAPABILITY AT DLR, Proc. of the 2004 Envisat & ERS Symposium, Salzburg, Austria.

Neusch, T. and Sties, M., 1999. Application of the Dubois-model using experimental synthetic aperture radar data for the determination of soil moisture and surface roughness. Isprs Journal of Photogrammetry and Remote Sensing, 54(4): 273-278.

NRCA, 2006. Crop Identification and Condition Mapping using Polarimetric SAR data http://ccrs.nrcan.gc.ca/radar/agri/crop_id/details_e.php.

Oh, Y. and Kay, Y.C., 1998. Condition for precise measurement of soil surface roughness. Ieee Transactions on Geoscience and Remote Sensing, 36(2): 691-695.

Oh, Y., Sarabandi, K. and Ulaby, F.T., 1992. An Empirical-Model and an Inversion Technique for Radar Scattering from Bare Soil Surfaces. Ieee Transactions on Geoscience and Remote Sensing, 30(2): 370-381.

Ping, X., 2003. Digital Elevation Model extraction from Aster In support of the "Coal fire and environmental research project, China". MSc Thesis, 71 pp.

Raney, R.K., 1998. Radar Fundamentals: Technical Perspective. In: F.M. Henderson and A.J. Lewis (Editors), Principles and Applications of Imaging Radar. John Wiley, New York, pp. 9-130.

Rosich, B. and Meadows, P., 2004. Absolute calibration of ASAR Level 1 products, ESA-ESRIN and BAE SYSTEMS Advanced Technology Centre.

Small, D., Meier, E. and Nüesch, D., 2004. Robust Radiometric Terrain Correction for SAR Image Comparisons, Proc. of CEOS SAR Calibration Workshop, Ulm, Germany.

SU, Z. and Troch, P.A.a.D.T., F. P., 1997. Remote sensing of bare surface soil moisture using EMAC/ESAR data. International Journal of Remote Sensing, 18(10): 2105-2124.

Trevett, J.W., 1986. Imaging Radar for Resources Surveys. Chapman and Hall, London, 313 pp.

Waring, R.H. et al., 1995. Biologists Toolbox - Imaging Radar for Ecosystem Studies. Bioscience, 45(10): 715-723.

Zobeck, T.M. and Onstad, C., A., 1987. Tillage and rainfall effects on random roughness a review. Soil Tillage Research, 9: 1-20.

Zribi, M., Baghdadi, N., Holah, N., Fafin, O. and Guerin, C., 2005. Evaluation of a rough soil surface description with ASAR-ENVISAT radar data. Remote Sensing of Environment, 95(1): 67-76.

Appendix-I

Table I-A   Description of GCP points before post-processing

Point id	"N" Latitude	"E" Longitude	Ellipsoidal Height	Pos. + Hgt. Qlty
Point- base01	30° 27' 13.34579"	77° 52' 42.36562"	651.8166	1.9097
point -01	30° 26' 48.05079"	77° 51' 20.99169"	566.5051	4.6253
point -02	30° 26' 31.76185"	77° 50' 17.24568"	522.3193	5.8223
point -03	30° 26' 15.51763"	77° 49' 37.69945"	497.157	7.7983
point -04	30° 25' 09.47354"	77° 49' 33.94615"	484.629	4.8067
point -05	30° 24' 40.76752"	77° 48' 44.22334"	457.5854	5.7787
point -06	30° 24' 21.04414"	77° 47' 37.92886"	423.4964	4.7183
ptbase01	30° 27' 13.29255"	77° 52' 42.37914"	649.5862	1.5841
point -07	30° 26' 16.29427"	77° 47' 49.37160"	445.7331	4.156
point -08	30° 25' 44.00633"	77° 47' 39.16678"	442.5715	3.8081
point -09	30° 23' 18.10054"	77° 48' 40.64032"	440.443	6.7904
point -10	30° 23' 58.47227"	77° 51' 13.36794"	511.1129	5.5857
point -11	30° 23' 40.00987"	77° 52' 12.80086"	537.6372	5.662
point -12	30° 23' 55.85995"	77° 52' 37.20655"	556.8437	5.5597
point -13	30° 24' 24.27882"	77° 54' 29.86524"	605.0032	5.6868
Point- base01	30° 27' 13.38332"	77° 52' 42.39196"	652.222	1.7886
point -14	30° 26' 36.99073"	77° 52' 51.34936"	637.4001	5.0665
point -15	30° 26' 15.64422"	77° 52' 53.78305"	645.6451	5.1818
point -16	30° 25' 42.40029"	77° 53' 13.31450"	653.9446	5.7667
point -17	30° 26' 17.55117"	77° 55' 29.92245"	851.5908	5.4124
point -18	30° 25' 06.24683"	77° 54' 38.70471"	689.009	5.9787
point -19	30° 26' 18.76975"	77° 55' 38.06738"	869.8312	5.1264
Point- base01	30° 27' 13.35941"	77° 52' 42.43132"	650.8376	2.0025
point -20	30° 28' 39.11053"	77° 48' 26.47351"	447.4159	4.1453
point -21	30° 28' 49.91576"	77° 47' 36.63080"	435.2812	5.0378
point -22	30° 27' 58.79881"	77° 45' 18.98087"	414.1664	5.3684
point -23	30° 25' 24.99000"	77° 46' 25.43989"	420.831	7.16

Table I-B Description of GCP points after post-processing using Skipro®

Point id	Northing	Easting	Ellip. Hgt.	Sd. Hgt.	Posn. Qlty.	Hgt. Qlty.	Posn. + Hgt. Qlty.
Pt-01	3372582.18	776404.52	660.18	0.1480	0.0928	0.1480	0.1747
point -01	3371747.65	774251.54	572.70	0.0068	0.0031	0.0068	0.0075
point -02	3371203.67	772563.96	527.90	0.0029	0.0015	0.0029	0.0033
point -03	3370677.94	771518.95	501.19	0.0037	0.0018	0.0037	0.0042
point -04	3368637.86	771472.16	492.95	0.0018	0.0011	0.0018	0.0021
point -05	3367720.98	770166.46	457.63	0.7135	0.3512	0.7135	0.7952
point -06	3367072.90	768412.72	433.11	0.0070	0.0034	0.0070	0.0078
Pt-01	3372580.13	776404.31	658.37	0.1018	0.0631	0.1018	0.1198
point -07	3370628.64	768628.73	455.19	0.0041	0.0020	0.0041	0.0045
point -08	3369623.85	768380.60	453.44	0.3372	0.2332	0.3372	0.4100
point -09	3365169.42	770134.61	445.81	0.3203	0.1590	0.3203	0.3576
point -10	3366519.83	774180.57	519.54	0.0034	0.0021	0.0034	0.0040
point -11	3365992.11	775781.22	545.57	0.0022	0.0012	0.0022	0.0025
point -12	3366493.74	776422.33	563.91	0.0020	0.0011	0.0020	0.0023
point -13	3367447.93	779408.11	611.20	0.0012	0.0008	0.0012	0.0014
Pt-01	3372583.10	776404.74	660.12	0.1347	0.0840	0.1347	0.1588
point -14	3371467.44	776670.94	644.60	0.0123	0.0078	0.0123	0.0145
point -15	3370813.54	776753.15	653.48	0.0016	0.0008	0.0016	0.0018
point -16	3369803.54	777300.74	656.12	0.0042	0.0017	0.0042	0.0046
point -17	3370978.35	780917.67	863.44	0.0033	0.0022	0.0033	0.0040
point -18	3368744.47	779609.60	685.55	0.2848	0.1211	0.2848	0.3095
point -19	3371022.00	781137.83	875.61	0.0035	0.0022	0.0035	0.0041
Pt-01	3372581.89	776406.00	660.17	0.1093	0.0679	0.1093	0.1287
point -20	3375050.66	769510.36	455.35	0.0025	0.0017	0.0025	0.0030
point -21	3375344.38	768170.47	437.43	0.4536	0.2054	0.4536	0.4980
point -22	3373684.28	764539.27	420.93	0.1396	0.0615	0.1396	0.1526
point -23	3368994.09	766427.48	420.78	0.3720	0.1863	0.3720	0.4160

Appendix-II

Table II-A: RMS crop height of paddy and observed backscattering coefficients (db values) for different incidence angles and polarizations for during monsoon datasets

Sl. No.	Rms crop height (Paddy)	Backscattering coefficients dB (values) for each swath and polarization									
		IS-2* (HH)	IS-2 (HV)	IS-4* (HH)	IS-4 (HV)	IS-6* (HH)	IS-6 (HV)	IS-2 (VH)	IS-2 (VV)	IS-4 (VH)	IS-4 (VV)
1	6.64	-12.91	-18.52	-7.8	-16.77	-5.77	-14.99	-17.02	-12.91	-17.86	-12.86
2	8.34	-7.42	-15.94	-6.33	-14.34	-4.23	-12.92	-15.16	-3.39	-17.78	-10.11
3	10.83	-20.42	-20.58	-4.85	-9.11	-3.62	-8.88	-16.83	-7.91	-22.36	-9.11
4	8.17	-10.64	-24.34	-13.78	-20.69	-11.94	-19.98	-10.18	-2.58	-14.93	-9.06
5	10.75	-12.94	-17.12	-11.55	-20.1	-10.49	-14.47	-23.49	-6.37	-18.22	-14.85
6	9.21	-11.34	-18.77	-13.18	-14.56	-6.22	-14.26	-11.12	-1.56	-17.87	-11.18
7	11.01	-10.07	-14.82	-11.56	-17.46	-11.73	-13.86	-16.97	-2.72	-12.81	-7.07
	Correlation Coefficient (R)	-0.4	0.3	-0.1	0.2	-0.2	0.5	-0.4	0.3	-0.1	0.2

* Incidence angle range for each Swath

IS-2 = 19.2 - 26.7^0 ,   IS-4 = 31.0 - 36.3^0 ,   IS-6 = 39.1 - 42.8^0

Table II-B: RMS crop height of maize and observed backscattering coefficients (db values) for different incidence angles and polarizations for during monsoon datasets

Sl. N o	Rms crop height maize	Backscattering coefficients dB (values) for each swath and polarization									
		IS-2 (HH)	IS-2 (HV)	IS-4 (HH)	IS-4 (HV)	IS-6 (HH)	IS-6 (HV)	IS-2 (VH)	IS-2 (VV)	IS-4 (VH)	IS-4 (VV)
1	29.17	-5.53	-16.10	-2.97	-16.35	-11.65	-18.41	-18.85	-6.90	-18.02	-9.32
2	39.58	-6.40	-10.13	-9.1	-13.07	-8.71	-14.04	-13.19	-2.39	-13.01	-10.21
3	31.69	-7.34	-8.53	-10.5	-16.13	-10.73	-17.74	-12.97	-3.67	-22.16	-4.92
5	27.24	-10.86	-19.93	-5.09	-10.25	-6.83	-16.91	-16.32	-15.77	-19.79	-10.66
7	29.65	-9.00	-15.93	-8.39	-12.59	-4.62	-15.25	-14.18	-13.85	-15.01	-10.37
8	71.76	-0.75	-12.88	-5.62	-12.68	-5.61	-11.79	-17.70	-11.38	-12.49	-8.5
9	61.72	-10.88	-17.77	-7.87	-13.62	-7.37	-8.50	-12.77	-9.99	-14.17	-3.96
13	37.09	-10.69	-12.35	-7.54	-14.93	-3.63	-11.03	-21.12	-17.69	-15.91	-7.98
15	40.72	-5.90	-9.32	-13.28	-23.61	-6.31	-12.73	-24.43	-11.44	-20.33	-11.56
17	34.50	-6.48	-20.73	-10.28	-16.47	-7.40	-9.42	-17.75	-10.83	-15.9	-7.95
18	26.07	-4.54	-13.19	-9.02	-10.38	-9.02	-10.38	-27.24	-15.94	-16.95	-13.97
20	42.78	-7.27	-14.52	-14.43	-16.07	-7.61	-12.58	-11.45	0.18	-15.16	-9.54
	Correlation Coefficient (R)	0.3	0.1	0.0	0.0	0.3	0.5	0.2	0.1	0.6	0.4

* Incidence angle range for each Swath

**Table II-C: RMS height of soil surface and observed backscattering coefficients (db values) for swath
IS-2 at VV and VH polarizations for post-monsoon session**

Field No.	RMS surface height	dB (values)	
		IS-2 (vh)	IS-2 (vv)
1	0.94	-19.92	-14.31
2	0.91	-16.50	-9.63
3	1.26	-11.02	-7.80
5	0.80	-18.03	-10.51
7	0.97	-15.17	-13.19
8	1.94	-12.72	-3.82
9	0.98	-18.42	-8.51
12	1.44	-16.06	-11.92
13	0.98	-19.38	-11.68
15	0.88	-17.30	-13.19
17	0.88	-13.99	-6.36
18	1.82	-10.83	-9.92
20	1.08	-16.90	-7.82
Correlation Coefficient (R)		0.7	0.4

**Table II-D: RMS height of soil surface and observed backscattering coefficients (db values) for swath
IS-6 at VV and VH polarizations for post-monsoon session**

Field No.	RMS surface Height	db(values)	
		IS-6 (vh)	IS-6 (vv)
1	0.81	-21.04	-14.37
2	1.56	-14.22	-10.45
3	1.26	-17.63	-12.16
5	0.79	-13.79	0.05
7	0.93	-15.36	-6.74
8	1.10	-15.28	-11.00
9	1.33	-13.55	-10.53
12	2.36	-10.49	-4.54
13	0.81	-12.83	-7.11
15	0.87	-16.22	-7.93
17	0.88	-14.89	-9.71
18	1.82	-13.00	-4.79
20	1.08	-12.56	-9.87
Correlation coefficient (R)		0.5	0.2

Table II-E: RMS height of soil surface and observed backscattering coefficients (db values) for swath IS-4 at HH and HV polarizations for post-monsoon session

Field No.	RMS surface height	db(values)	
		IS-4 (hh)	IS-4 (hv)
7	0.93	-5.46	-12.36
8	1.10	-10.10	-15.84
9	1.33	-8.12	-11.76
12	2.36	-8.58	-18.47
13	0.81	-7.37	-12.47
15	0.87	-12.72	-15.18
17	0.88	-11.59	-15.51
18	1.82	-6.97	-15.12
20	1.08	-10.21	-15.30
Correlation coefficient (R)		0.3	-0.6

Table II-F: RMS height of soil surface and observed backscattering coefficients (db values) for swath IS-6 at HH and HV polarizations for post-monsoon session

Field No.	RMS surface height	db(values)	
		IS-6 (hh)	IS-6 (hv)
1	0.86	-13.50	-17.05
2	0.94	-10.71	-13.23
3	0.82	-8.09	-18.07
5	0.82	-10.54	-18.64
7	0.93	-9.12	-21.83
8	1.10	-6.21	-14.25
9	1.33	-9.09	-12.47
12	2.37	-15.22	-20.60
13	0.81	-11.07	-16.78
15	1.39	-10.80	-15.05
17	0.88	-10.97	-16.22
18	0.90	-11.40	-15.07
20	1.08	-9.24	-17.05
Correlation coefficient (R)		-0.5	-0.2

Table II-G: RMS crop height of paddy and observed backscattering coefficients (db values) for different incidence angles and polarizations for post-monsoon datasets

Field No.	RMS crop height (paddy)	Backscattering coefficients dB (values) for each swath and polarization							
		IS-2 (vh)	IS-2 (vv)	IS-6 (vh)	IS-6 (vv)	IS-4 (hh)	IS-4 (hv)	IS-6 (hh)	IS-6 (hv)
4	53.7755	-15.738	-3.820	-13.55	-7.47	-	-	-11.98	-16.34
6	14.4049	-19.771	-10.943	-12.78	-5.78	-	-	-7.84	-17.26
10	16.4104	-20.235	-11.389	-11.72	-5.31	-11.88	-19.71	-12.99	-16.98
11	21.7071	-19.306	-11.768	-11.84	-8.88	-4.36	-16.33	-18.81	-19.52
14	20.1296	-16.965	-7.320	-16.10	-10.59	-9.03	-14.04	-8.42	-15.42
16	20.8039	-19.106	-4.597	-20.96	-11.10	-6.89	-20.93	-10.29	-12.75
19	13.3154	-12.084	-12.349	-21.88	-13.85	-12.04	-19.82	-12.26	-16.09
21	18.3780	-13.618	-9.536	-23.42	-18.43	-11.37	-16.80	-14.35	-12.14
Correlation Coefficient (R)		0.1	0.7	0.3	0.2	0.8	0.4	-0.1	-0.1

Table II-H: Volumetric moisture content in maize fields and observed backscattering coefficients (db values) for swath IS-2 at HH and HV polarizations for during-monsoon datasets

Field No.	VMC (5cm)	VMC (10cm)	IS-2 dB(HH)	IS-2 dB(HV)
1	13.95	15.44	-5.53	-16.10
2	19.33	19.20	-6.40	-10.13
3	17.19	19.45	-7.34	-8.53
5	11.41	14.04	-10.86	-19.93
7	16.86	17.73	-9.00	-15.93
8	14.22	14.36	-0.75	-12.88
9	11.03	14.18	-10.88	-17.77
13	12.76	17.76	-10.69	-12.35
15	17.78	16.15	-5.90	-9.32
17	8.58	13.60	-6.48	-20.73
18	17.39	17.02	-4.54	-13.19
20	12.33	14.76	-7.27	-14.52
Correlation coefficient (R) HH	0.3	-0.1		
Correlation coefficient (R) HV	0.8	0.8		

Table II-I: Volumetric moisture content in maize fields and observed backscattering coefficients (db values) for swath IS-4 at HH and HV polarizations for during-monsoon datasets

Field_id	VMC (5cm)	VMC (10cm)	IS-4 dB(HH)	IS-4 dB(HV)
1	15.48	18.38	-2.97	-16.35
2	17.09	20.27	-9.10	-13.07
3	20.64	23.02	-10.50	-16.13
5	17.14	18.46	-5.09	-10.25
7	17.31	14.17	-8.39	-12.59
8	17.33	20.66	-5.62	-12.68
9	15.56	16.79	-7.87	-13.62

Field_id	VMC (5cm)	VMC (10cm)	IS-4 dB(HH)	IS-4 dB(HV)
13	18.33	19.93	-7.54	-14.93
15	18.66	24.98	-13.28	-23.61
17	14.98	15.30	-10.28	-16.47
18	Irrigation was in progress			
20	14.18	20.51	-14.43	-16.07
Correlation coefficient (R) HH	0.0	-0.4		
Correlation coefficient (R) HV	-0.2	-0.6		

Table II-J: Volumetric moisture content in maize fields and observed backscattering coefficients (db values) for swath IS-6 at HH and HV polarizations for during-monsoon datasets

Field_id	VMC (5cm)	VMC (10cm)	IS-6 dB(HH)	IS-6 dB(HV)
1	11.28	16.91	-11.65	-18.41
2	17.75	26.07	-8.71	-14.04
3	19.21	20.60	-10.73	-17.74
5	13.73	16.63	-6.83	-16.91
7	12.72	15.07	-4.62	-15.25
8	14.47	33.66	-5.61	-11.79
9	20.45	28.61	-7.37	-8.50
13	16.57	20.58	-3.63	-11.03
15	21.83	26.82	-6.31	-12.73
17	16.73	16.93	-7.40	-9.42
18	19.15	19.88	-9.02	-10.38
20	14.13	18.35	-7.61	-12.58
Correlation coefficient (R) HH	0.0	0.2		
Correlation coefficient (R) HV	0.5	0.4		

Table II-K: Volumetric moisture content in maize fields and observed backscattering coefficients (db values) for swath IS-2 at VH and VV polarizations for during-monsoon datasets

Field_id	VMC (5cm)	VMC (10cm)	IS-2 dB(VH)	IS-2 dB(VV)
1	15.75	19.05	-18.85	-6.90
2	22.92	20.49	-13.19	-2.39
3	22.81	19.81	-12.97	-3.67
5	15.36	15.85	-16.32	-15.77
7	17.78	15.85	-14.18	-13.85
8	18.72	18.59	-17.70	-11.38
9	12.95	15.24	-12.77	-9.99
13	14.12	17.53	-21.12	-17.69
15	21.22	19.51	-24.43	-11.44
17	15.99	14.69	-17.75	-10.83
18	11.30	16.17	-27.24	-15.94
20	12.68	15.45	-11.45	0.18
Correlation coefficient (R) VH	0.2	-0.1		
Correlation coefficient (R) VV	0.4	0.3		

Table II-L: Volumetric moisture content in maize fields and observed backscattering coefficients (db values) for swath IS-4 at VH and VV polarizations for during-monsoon datasets

Field_id	VMC (5cm)	VMC (10cm)	IS-4 dB(VH)	IS-4 dB(VV)
1	13.95	15.44	-18.02	-9.32
2	19.33	19.20	-13.01	-10.21
3	17.19	19.45	-22.16	-4.92
5	11.41	14.04	-19.79	-10.66
7	16.86	17.73	-15.01	-10.37
8	14.22	14.36	-12.49	-8.50
9	11.03	14.18	-14.17	-3.96
13	12.76	17.76	-15.91	-7.98
15	17.78	16.15	-20.33	-11.56
17	8.58	13.60	-15.90	-7.95
18	17.39	17.02	-16.95	-13.97
20	12.33	14.76	-15.16	-9.54
Correlation coefficient (R) VH	-0.1	-0.2		
Correlation coefficient (R) VV	-0.4	-0.1		

Table II-M: Volumetric moisture content in maize fields and observed backscattering coefficients (db values) for swath IS-2 at VH and VV polarizations for post-monsoon datasets

Field_id	VMC (5cm)	VMC (10cm)	IS- 2 db(VH)	IS-2 db(VV)
1	6.69	10.19	-19.92	-14.31
2	10.46	12.30	-16.50	-9.63
3	8.46	10.24	-11.02	-7.80
5	9.17	10.25	-18.03	-10.51
7	11.39	11.44	-15.17	-13.19
8	14.22	14.18	-12.72	-3.82
9	12.90	14.61	-18.42	-8.51
12	9.97	12.43	-16.06	-11.92
13	12.17	13.08	-19.38	-11.68
15	15.60	15.61	-17.30	-13.19
17	9.36	10.10	-13.99	-6.36
18	10.27	10.53	-10.83	-9.92
20	10.07	11.15	-16.90	-7.82
Correlation coefficient (R) VH	0.0	-0.3		
Correlation coefficient (R) VV	0.1	0.0		

Table II-N: Volumetric moisture content in maize fields and observed backscattering coefficients (db values) for swath IS-6 at VH and VV polarizations for post-monsoon datasets

Field_id	VMC (5cm)	VMC (10cm)	IS-6 db(VH)	IS-6 db(VV)
1	6.73	7.51	-21.04	-14.37
2	10.58	12.23	-14.22	-10.45
3	9.36	11.58	-17.63	-12.16
5	10.10	10.79	-13.79	0.05
7	9.13	11.15	-15.36	-6.74
8	5.59	7.39	-15.28	-11.00

Field_id	VMC (5cm)	VMC (10cm)	IS-6 db(VH)	IS-6 db(VV)
9	4.19	5.54	-13.55	-10.53
12	5.96	7.96	-10.49	-4.54
13	4.14	7.11	-12.83	-7.11
15	12.08	15.11	-16.22	-7.93
17	6.53	7.04	-14.89	-9.71
18	7.10	9.25	-13.00	-4.79
20	4.20	4.53	-12.56	-9.87
Correlation coefficient (R) VH	-0.3	-0.3		
Correlation coefficient (R) VV	0.2	0.2		

Table II-O: Volumetric moisture content in maize fields and observed backscattering coefficients (db values) for swath IS-4 at HH and HV polarizations for post-monsoon datasets

Field_id	VMC (5cm)	VMC (10cm)	IS-4 db(HH)	IS-4 db(HV)
7	5.43	8.86	-5.46	-12.36
8	8.35	10.30	-10.10	-15.84
9	6.78	5.94	-8.12	-11.76
12	5.48	8.03	-8.58	-18.47
13	5.59	9.52	-7.37	-12.47
15	11.88	13.90	-12.72	-15.18
17	10.33	10.23	-11.59	-15.51
18	4.65	11.53	-6.97	-15.12
20	4.90	7.27	-10.21	-15.30
Correlation coefficient (R) HH	-0.81	-0.41		
Correlation coefficient (R) HV	-0.14	-0.24		

Table II-P: Volumetric moisture content in maize fields and observed backscattering coefficients (db values) for swath IS-6 at HH and HV polarizations for post-monsoon datasets

Field_id	VMC (5cm)	VMC (10cm)	IS-6 db(HH)	IS-6 db(HV)
1	8.83	11.63	-13.50	-17.05
2	16.49	19.50	-10.71	-13.23
3	11.20	14.45	-8.09	-18.07
5	10.62	10.80	-10.54	-18.64
7	13.04	12.47	-9.12	-21.83
8	10.52	13.55	-6.21	-14.25
9	14.51	17.41	-9.09	-12.47
12	10.12	12.43	-15.22	-20.60
13	12.34	15.57	-11.07	-16.78
17	7.70	8.43	-10.97	-16.22
18	11.68	14.39	-11.40	-15.07
20	9.98	12.97	-9.24	-17.05
Correlation coefficient (R) HH	0.2	0.2		
Correlation coefficient (R) HV	0.4	0.6		